PREPRINT (LBNL Report)
to appear in: “THz Spectroscopy: Principles and Applications”
Susan L. Dexheimer, Editor, Taylor & Francis CRC Press (2007)

Time-resolved THz studies of carrier dynamics in semiconductors, superconductors, and strongly-correlated electron materials

Robert A. Kaindl

Lawrence Berkeley National Laboratory
Materials Sciences Division
1 Cyclotron Road,MS 2-350
Berkeley, CA 94720
RAKaindl@lbl.gov

Richard D. Averitt*

Boston University
Department of Physics
590 Commonwealth Ave.
Boston, MA 02215
raveritt@physics.bu.edu

*written while at Los Alamos National Laboratory

TABLE OF CONTENTS

1. INTRODUCTION

Perhaps the most important aspect of contemporary condensed matter physics involves understanding strong Coulomb interactions between the large number of electrons in a solid. Electronic correlations lead to the emergence of new system properties, such as metal-insulator transitions, superconductivity, magneto-resistance, Bose-Einstein condensation, the formation of excitonic gases, or the integer and fractional Quantum Hall effects. The discovery of high-T_C superconductivity in particular was a watershed event, leading to dramatic experimental and theoretical advances in the field of correlated-electron systems.[1-10] Such materials often exhibit competition between the charge, lattice, spin, and orbital degrees of freedom, whose cause-effect relationships are difficult to ascertain. Experimental insight into the properties of solids is traditionally obtained by time-averaged probes, which measure e.g. linear optical spectra, electrical conduction properties, or the occupied band structure in thermal equilibrium. Many novel physical properties arise from excitations out of the ground state into energetically higher states by thermal, optical, or electrical means. This leads to fundamental interactions between the system's constituents, such as electron-phonon and electron-electron interactions, which occur on ultrafast timescales. While these interactions underlie the physical properties of solids, they are often only indirectly inferred from time-averaged measurements.

Time-resolved spectroscopy, consequently, is playing an ever increasing role to provide insight into light-matter interaction, microscopic processes, or cause-effect relationships that determine the physics of complex materials. In the past, experiments using visible and near-infrared femtosecond pulses have been extensively employed, e.g. to follow relaxation and dephasing processes in metals and semiconductors.[11,12] However, many basic excitations in strongly-correlated electron systems and nanoscale materials occur at lower energies. The terahertz (THz) regime is particularly rich in such fundamental resonances. This includes ubiquitous lattice vibrations and low-energy collective oscillations of conduction charges. In nanoscale materials, band structure quantization also yields novel infrared and THz transitions, including intersubband absorption in quantum wells. The formation of excitons in turn leads to low-energy excitations analogous to inter-level transitions in atoms. In transition-metal oxides, fundamental excitation gaps arise from charge pairing into superconducting condensates and other correlated states. This motivates the use of ultrafast THz spectroscopy as a powerful tool to study light-matter interactions and microscopic processes in nanoscale and correlated-electron materials.

A distinct advantage of coherent THz pulses is that the amplitude *and* phase of the electric field can be measured directly, as the THz fields are coherent with the fs pulses from which they are generated. Using THz time-domain spectroscopy (THz-

TDS), both the real and imaginary parts of the response functions, such as the dielectric function $\varepsilon(\omega) = \varepsilon_1(\omega) + i\varepsilon_2(\omega)$, are obtained directly without the need for Kramers–Kronig transforms.[13] The THz response can also be expressed in terms of absorption $\alpha(\omega)$ and refractive index $n(\omega)$, or as the optical conductivity $\sigma(\omega) \equiv \sigma_1(\omega) + i\sigma_2(\omega) = i\omega\varepsilon_0[1-\varepsilon(\omega)]$. The conductivity $\sigma(\omega)$ describes the current response $J(\omega) = \sigma(\omega)E(\omega)$ of a many-body system to an electric field, an ideal tool to study conducting systems. A second important advantage is the ultrafast time resolution that results from the short temporal duration of the THz time-domain sources. In particular, optical-pump THz-probe spectroscopy enables a delicate probe of the transient THz conductivity after optical photoexcitation. These experiments can provide insight into quasiparticle interactions, phase transitions, or nonequilibrium dynamics. In this chapter we will provide many such examples.

Since THz spectroscopy of solids is a quickly expanding field of research, we must define a limited scope to be covered in this chapter. We will review studies of semiconductors, superconductors, and strongly-correlated electron systems using few-cycle infrared pulses that are accessible to direct field-resolved detection. This entails a photon energy range from below 4 meV (≈ 1 THz) to about 100 meV. We specifically omit measurements with "conventional" time-averaged techniques such as Fourier-transform infrared spectroscopy,[1,14] and we will skip over experiments that are covered elsewhere in this book, such as THz studies of semiconductor nanocrystals or THz sideband generation on intersubband transitions.

In Section 2, we discuss quasiparticle dynamics in bulk semiconductors and nanostructured materials such as GaAs quantum wells. This includes the free carrier response, the formation of quasiparticles, intra-excitonic spectroscopy, and the nonlinear response of intersubband transitions. In Section 3, we consider the THz response and dynamics in conventional superconductors, and in the high-T_C superconductors YBCO and Bi-2212. As we will show, with optical-pump THz-probe spectroscopy it is possible to simultaneously monitor quasiparticle and superconducting condensate fractions with sub-ps temporal resolution. Dynamics in half-metallic transition-metal oxides $LaCaMnO_3$ and in the pyrochlore $Tl_2Mn_2O_7$ are presented in Section 4. Colossal magnetoresistance is observed in both materials, and time-resolved THz spectroscopy provides insight into the relevance of the spin degree of freedom for charge transport and carrier lifetimes. Finally, in Section 5, we provide a summary and offer suggestions for future experiments on nanoscale and correlated-electron materials using time-resolved THz spectroscopy.

2. BULK AND NANOSTRUCTURED SEMICONDUCTORS

2.1 OVERVIEW

In this section, we review low-energy excitations and carrier dynamics in bulk and nanostructured semiconductors as detemined via coherent THz spectroscopy. The revolutionary impact of semiconductors on modern technology goes hand in hand with an extremely high, atomic-scale precision in their manufacture, and with an immensely detailed knowledge of their physical properties which is presently unattainable for the strongly-correlated electron systems discussed in later sections. This makes semiconductors an ideal testing ground for novel physical concepts and experiments, and for tailored opto-electronic devices. Femtosecond laser pulses in the visible and near-IR have been extensively used to study photoexcited carriers in semiconductors. Such pulses are resonant to the typically 1-2 eV band gaps. Experiments have progressed from pump-probe and luminescence to modern multi-dimensional coherent spectroscopies which all provide deep insight into relaxation timescales, inter-band coherences, or many-body correlations.[11,12,15] As we will show in this section, semiconductors provide equally interesting and fundamental excitations at energies far below their valence-to-conduction band gaps. Here, time-domain THz and optical-pump THz-probe studies are powerful techniques to discern excitations that remain inaccessible to visible light and to probe conduction processes at frequencies comparable to relaxation processes in these materials.

2.2 FREE CARRIER DYNAMICS IN BULK SEMICONDUCTORS

The simplest description of free carriers in response to an applied electric field in a doped or photoexcited semiconductor (or other conducting material) is given by the Drude model. In this model, carriers elastically scatter with a rate τ^{-1}. The complex Drude conductivity is given as

$$\sigma(\omega) = \frac{\sigma_{DC}}{1 - i\omega\tau} \tag{1}$$

where the DC conductivity σ_{DC} is given by

$$\sigma_{DC} \equiv ne^2\tau / m^* = ne\mu = \varepsilon_0 \omega_p^2 \tau. \tag{2}$$

In this equation, n is the carrier density, τ the collision time, m^* the effective mass, μ the mobility, ε_0 the free space permittivity and ω_p the bare plasma frequency. While the Drude response can be derived from very simple considerations, it is important to emphasize that its validity is much broader. In fact, the Drude response can be derived from the semi-classical Boltzmann transport equation and even more

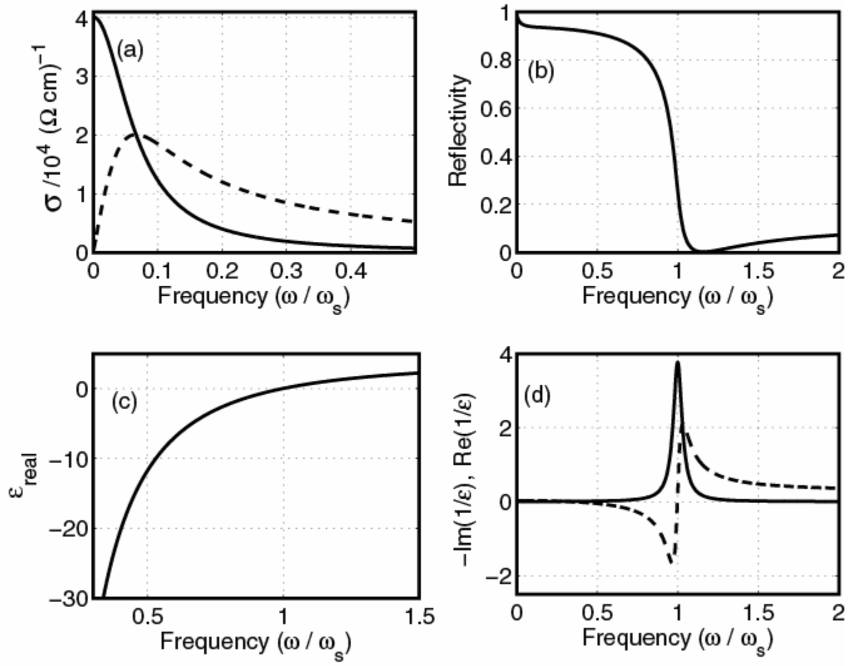

Fig. 1 Example of the Drude response plotted in terms of **(a)** the real part (solid line) and imaginary part (dashed) of the complex conductivity $\sigma(\omega)$, **(b)** the reflectivity $R(\omega)$, **(c)** the real part $\varepsilon_1(\omega)$ of the permittivity, and **(d)** the loss function shown as $-\mathrm{Im}(1/\varepsilon)$ (solid line) and $\mathrm{Re}(1/\varepsilon)$ (dashed). Frequencies are scaled to the screened plasma frequency $\omega_s = \omega_p/\sqrt{\varepsilon_\infty}$.

rigorously from Kubo-Greenwood formalism.[16] For example, using a Boltzmann approach, it is easy to show that

$$\sigma_{DC} = \frac{e^2}{12\pi^3\hbar}\left\langle \lambda_F \right\rangle S_F \tag{3}$$

where $\langle\lambda_F\rangle$ is the mean free path averaged over the Fermi surface, and S_F is the area of the Fermi surface. For a spherical Fermi surface this is equivalent to the Drude result highlighting that the relevant electrons are those at the Fermi surface with velocity v_F.

The Drude model serves as a useful starting point for understanding the properties and time evolution of many materials, as we will see time and again throughout this chapter. In superconductors, for instance, the spectral weight associated with a normal state Drude response downshifts into a zero-frequency δ-function associated with the superconducting condensate upon cooling below the transition temperature T_C. In manganites, the Drude spectral weight is in transferred to higher energies as phonon and spin fluctuations transform the coherent free carrier response into a hopping-like polaronic response. In this sense, *changes* in the Drude response due to thermal or nonequilibrium perturbations serve as a sensitive probe of interactions or the onset of correlations. Deviations from the Drude model are, of course, often observed. They have been treated e.g. via a frequency-dependent scattering rate[17] or a distribution of scattering times,[18] but the Drude model is an essential staring point even in these cases.

In the literature (and throughout this chapter) the Drude response is plotted in various ways. Figure 1 shows the calculated Drude response as a function of reduced frequency ω/ω_s where ω_s is the screened plasma frequency ($\omega_s = \omega_p /\surd\varepsilon_\infty$) for $\sigma_{DC} = 4\times10^4\ \Omega^{-1}\text{cm}^{-1}$, $\tau = 200$ fs, $\omega_p = 0.1$ eV, and $\varepsilon_\infty = 4$. The complex conductivity is plotted in Fig. 1(a), with the real part $\sigma_1(\omega)$ shown as the solid line and the imaginary part $\sigma_2(\omega)$ by the dashed line. Note that $\sigma_2(\omega) = \sigma_1(\omega) / 2$ at $1/\tau$, which provides a direct intuitive measure of the scattering rate. Figure 1(b) shows the corresponding reflectivity *R*, which drops dramatically at ω_s where the electrons no longer respond to the applied field. At higher frequencies, *R* rises again to the value $(1 - \surd\varepsilon_\infty)^2 / (1 + \surd\varepsilon_\infty)^2$. Quite often, the real part of $\varepsilon(\omega)$ is plotted as in Fig. 1(c), where it is negative below ω_s increasing to ε_∞ at higher frequencies. Finally, the Drude response is sometimes displayed as in Fig. 1(d), where the loss function $-\text{Im}(1/\varepsilon(\omega))$ peaks at the plasma frequency ω_s with a line width $1/\tau$.

As an example of a Drude-like response, Fig. 2 shows the results of THz-TDS measurements on lightly doped silicon[19], with carrier density $n \approx 10^{15}$ cm^{-3}. Figure 2(a) displays the real conductivity $\sigma_1(\omega)$ for *n*-type and *p*-type samples with the corresponding imaginary conductivity $\sigma_2(\omega)$ displayed in (b). This data highlights some specific advantages of THz-TDS. As mentioned earlier, the time-domain THz measurement provides the real and imaginary parts of $\sigma(\omega)$ directly. Moreover, the signal-to-noise in THz-TDS is sufficient to test various conductivity models. For both the *n*-type and *p*-type samples, the response cannot be fully explained with the Drude mode. Rather, the best experimental fit is obtained with the Cole-Davidson model

$$\sigma(\omega) = \frac{\sigma_{DC}}{\left(1 - i\omega\tau\right)^{\beta}}\,. \tag{4}$$

Here, β describes a distribution of relaxation times, such that the average scattering time $\langle\tau\rangle$ is given by $\tau\beta$ (Ref. 19). Thus, $\beta = 1$ reduces to the Drude response. For the data in Fig. 2, a best fit was obtained with $\beta = 0.84$ (0.76) for the *n*-type (*p*-type) samples. In Ref. 19, the pure Drude response (i.e. $\beta = 1$) was obtained for samples with somewhat higher carrier densities around $\approx 10^{17}$ cm^{-3}.

With optical-pump THz-probe spectroscopy, measurements of the Drude conductivity upon photoexcitation of electron-hole pairs have been performed by several groups.[20-22] Some experiments are described in more detail in the chapter by Schmuttenmaer. One example of a photoinduced Drude-like response we would like

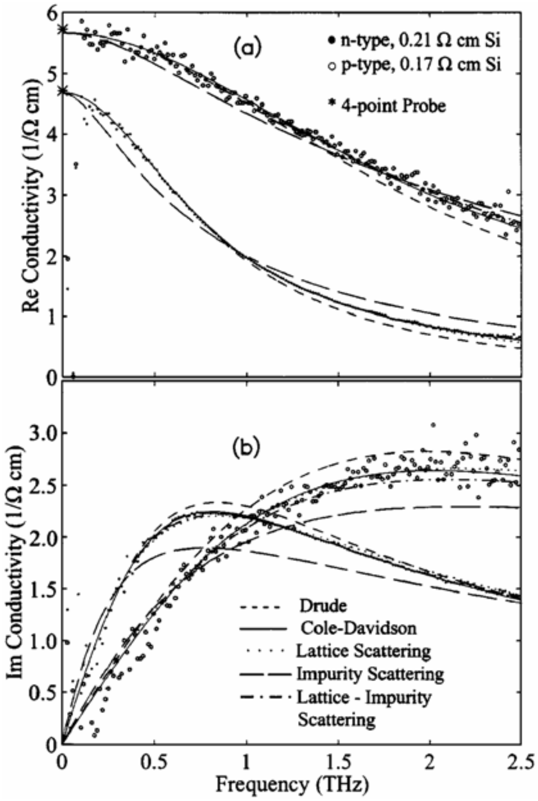

Fig. 2 Terahertz conductivity of *n*-type and *p*-type doped silicon, showing **(a)** the real part $\sigma_1(\omega)$ and **(b)** the imaginary part $\sigma_2(\omega)$. Lines: fits to various "Drude-like" conductivity models as indicated. Reprinted figure with permission from Ref. 19 © 1997 by the American Physical Society.

to highlight are the results on GaAs from Ref. 23. These results provide a striking example of the ultrafast evolution of the THz response during the development of many-body correlations following photoexcitation. In this experiment, pulses with 1.55 eV photon energy and approximately10 fs duration excited an electron-hole (*e*-*h*) plasma at a density of 10^{18} cm^{-3}. Monitoring the dynamics requires THz probe pulses with sufficient temporal resolution and with a spectral bandwidth extending beyond 40 THz. This was achieved using a scheme based on difference-frequency generation in GaSe combined with ultrabroadband free-space electro-optic sampling.[23-25]

The experimental results are displayed in Fig. 3, where the THz spectra of the dynamic loss function $1/\varepsilon(\omega,\tau_D)$ are plotted at various delays τ_D between the optical pump and THz probe pulses. The imaginary part of $1/\varepsilon(\omega,\tau_D)$ is plotted in panel (a) and the real part in panel (b). This is a particularly useful form to display the data as it highlights what this experiment is actually measuring. Namely, the evolution of particle interactions from a bare Coulomb potential V_q to a screened interaction

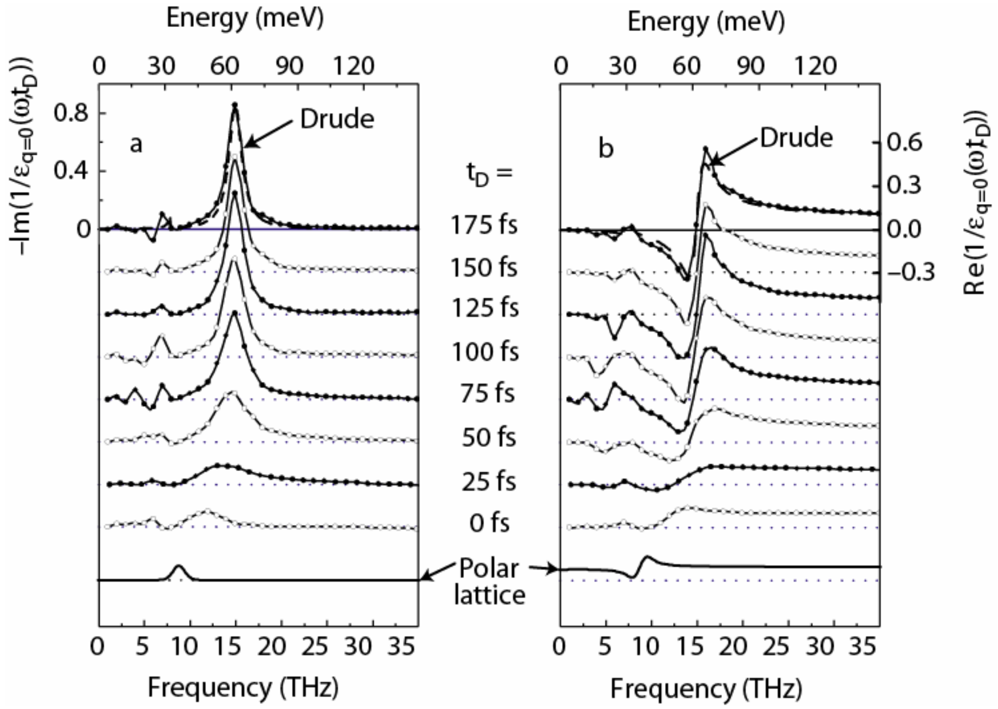

Fig. 3 Quasiparticle formation in GaAs following excitation with 10 fs 1.55 eV pulses. The dynamic loss function is plotted as a function of frequency at various delays following photoexcitation. The dynamic response evolves to a coherent Drude response on a timescale of ~175 fs as dressed quasiparticles are formed from an initially uncorrelated state at zero delay. Reprinted with permission from Ref. 23.

potential $W_q(\omega,\tau_D)$, where q is the momentum exchange between two particles during a collision:

$$V_q = \frac{4\pi e^2}{q^2} \quad \longrightarrow \quad W_q(\omega,\tau_d) \equiv \frac{V_q}{\varepsilon_q(\omega,\tau_d)}. \tag{5}$$

In essence, V_q becomes renormalized by the longitudinal dielectric function leading to a retarded response associated with the polarization cloud about the carriers. This is a many-body resonance at the plasma frequency ω_s and as described previously in Fig. 1(d), the loss function peaks at ω_s with a width corresponding to the scattering rate. Thus, the results of Fig. 3 show the evolution at $q = 0$ from an uncorrelated plasma to a many-body state with a well-defined collective plasmon excitation. This is evident in Fig. 3(a) where, prior to photoexcitation, there is a well-defined peak at 36 meV corresponding to polar optical phonons. Following photoexcitation, a broad resonance appears at higher energies that evolves on a 100 fs timescale into a narrow plasma resonance centered at 14.5 THz. The response is described by the Drude model only at late delay times. These results are consistent with quantum kinetic theories describing nonequilibrium Coulomb scattering.[23]

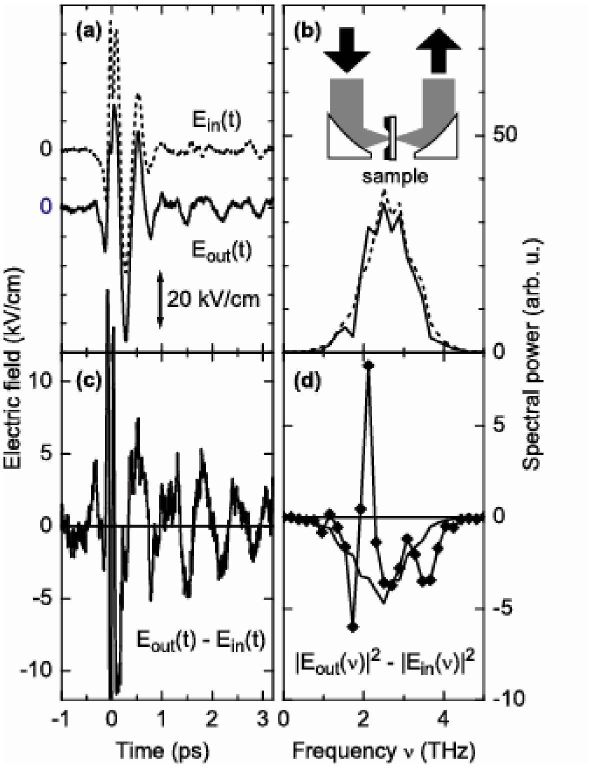

Fig. 4 Nonlinear THz transmission through GaAs. **(a)** Incident and transmitted pulses in the time domain and **(b)** corresponding spectrum of the pulses. **(c)** Time-domain difference between the incident and transmitted pulses clearly highlighting the oscillations following the main transient. In **(d)** the solid line is the difference in spectral power for low peak field transmission while the diamonds show high peak field results. Reprinted figure with permission from Ref. 30. © 2006 by the American Physical Society.

As a further example related to free carriers in doped semiconductors, we consider the response at high THz electric fields[26] with $E > 100$ kV/cm. Several groups are pursuing high-field THz generation using various approaches including large aperture photoconductors,[27] polaritons,[28] or transition radiation at the plasma-vacuum boundary.[29] A recently developed technique based on four-wave-mixing of the fundamental and second-harmonic of a Ti:sapphire laser has been used to generate THz pulses with peak field strengths greater than 400 kV/cm. In Ref. 26, amplified near-infrared pulses with 25 fs duration were focused into nitrogen with a 100 μm BBO crystal placed before the focus. The fundamental and second harmonic interact at the focus through a $\chi^{(3)}$ process to efficiently generate THz radiation. This source of THz radiation was subsequently utilized to induce a nonlinear response in *n*-type GaAs chemically doped to a carrier density of 10^{17}cm^{-3} (Ref. 30). In this experiment, the transmission of high peak field THz pulses (E >50 kV/cm) was compared to the transmission of lower field strength THz pulses (<1 kV/cm). Fig. 4(a) shows the incident and transmitted THz electric field in the time domain, and Fig. 4(b) displays the corresponding spectra. The sample is placed at the focus of an off-axis parabola (inset). In Fig. 4(c), the difference between incident and transmitted pulses reveals a 500 fs oscillation persisting after the main THz transient. This is more striking in the frequency domain, plotted as the difference in spectral power in Fig. 4(d). The solid line shows the low-field THz response, where the data is negative at all frequencies as expected for a Drude response. In contrast, for the high-field response (diamonds), a strong increase in the spectral power is observed over a narrow frequency range around 2 THz. This result could be explained in terms of the super-radiant decay of optically inverted impurity transitions in bulk GaAs. In this novel process that occurs at high THz fields, the incident field strength is sufficient to ionize a significant fraction of *s*-like neutral donors through excitation into continuum states. A fraction of the excited carriers are subsequently scattered to *p*-like impurity states, followed by stimulated emission of dipole allowed *p* → *s* transitions. A calculation based on a single-particle Schrödinger equation with randomly distributed donors is consistent with this interpretation.

2.3 INTRA-EXCITONIC SPECTROSCOPY

Bound *e-h* pairs (excitons) bring about strong modifications of the optical and electronic properties of semiconductors. Sharp exciton lines in the visible or near-IR are often observed around the band gap, which provides the basis for the widely employed absorption and luminescence studies based on exciton photo-generation and annihilation.[12,31] This contrasts sharply with *intra-excitonic* resonances,[32,33] which are low-energy electromagnetic transitions between internal exciton levels as illustrated in Fig. 5(a). Since exciton binding energies typically range between 1−100 meV, intra-excitonic transitions occur at THz frequencies. The sensitivity to transitions within *existing* exciton populations makes them an ideal tool to probe the absolute pair densities and the low-energy structure of excitonic gases. This differs from near-IR absorption and luminescence studies, which couple strongly to only a subset of states around $K \approx 0$ (optical light cone) due to momentum conservation, and are thus dependent on both exciton density and the energy distribution functions in a complex way. Since intra-excitonic transitions are due to changes of the relative momentum of the *e-h* pair, they can occur at much larger center-of-mass momenta K outside the visible light cone. Moreover, as discussed below so-called "dark excitons" with a forbidden inter-band dipole moment are easily accessible via intra-excitonic spectroscopy. These arguments strongly motivate the use of intra-excitonic THz probes as new tools for exciton spectroscopy.

Intra-excitonic spectroscopy is a rising field with an increasing breadth of applications. Early studies took advantage of the long recombination times in indirect semiconductors such as Ge, which enabled measurements using conventional infrared

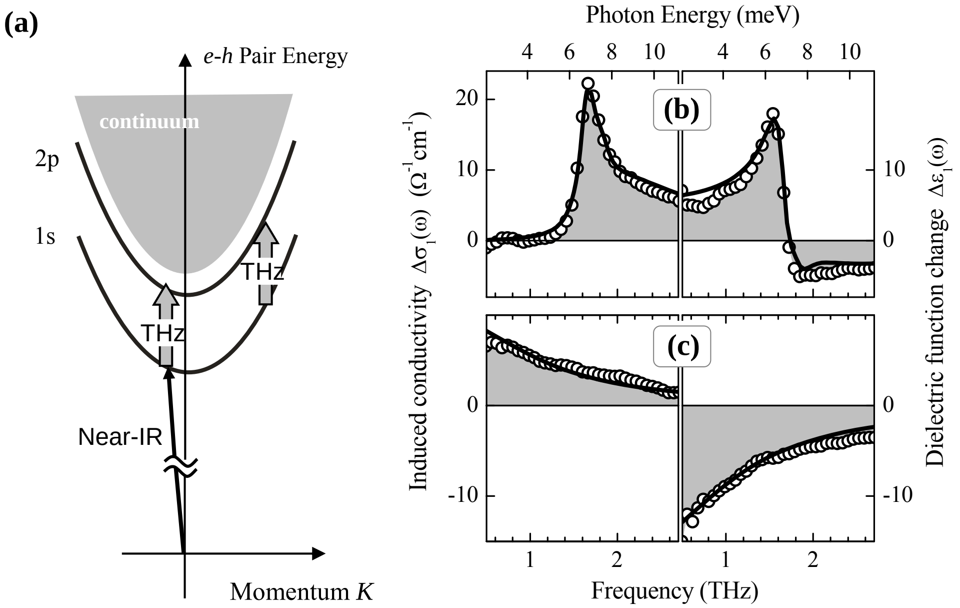

Fig. 5 Intra-excitonic spectroscopy. **(a)** Schematic dispersion of excitons and unbound *e-h* pairs along their center-of-mass momentum. Arrows indicate near-IR photogeneration of excitons, as well as intra-excitonic 1*s*-2*p* transitions. **(b)** Measured THz response in GaAs quantum wells (circles) 5 ps after resonant excitation at the 1*s* HH exciton line, at low temperature (T= 6 K). Lines: intra-excitonic model curve for density 3×10^{10} cm^{-2}. **(c)** Response after non-resonant excitation into the continuum at T = 300 K. In the experiments, photoexcitation of free carriers in the substrate was avoided by etching off the substrate, leaving only the quantum well structure and surrounding cladding layer attached to a THz-transmittive MgO substrate.

spectrometers.[34] The development of modern time-resolved THz spectroscopy gives access to a much larger range of materials, and enables studies of the ultrafast dynamics of excitons via intra-excitonic probes.[35-38] Their use to study fundamental exciton physics is strongly supported by recent microscopic calculations, which contrast the information gained to that of luminescence and predict significant changes of the THz spectrum in low-temperature excitonic phases.[39-41]

In the following, we first discuss optical-pump THz-probe experiments which detect intra-excitonic resonances in order to directly observe exciton formation and ionization dynamics.[37] These experiments were performed on a GaAs multiple-quantum well sample, which at lowest temperatures (6 K) exhibits a sharp near-IR absorption line of 1*s* heavy-hole (HH) excitons followed by higher-bound exciton lines and the broadband continuum. A 250-kHz regenerative Ti:sapphire amplifier delivering 150-fs pulses at 800 nm was used to generate and probe THz pulses in the 2-12 meV range via optical rectification and electro-optic sampling in 500-µm thick ZnTe crystals. The high repetition rate of this setup provides both sensitive detection with 10^4:1 signal-to-noise ratio in the THz electric field and sufficiently high, µJ pulse energies to photoexcite the large THz probe areas. Near-IR pump pulses were spectrally narrowed to 2 meV and tuned to selectively excite either the sharp 1*s* exciton line or the continuum of unbound *e-h* pairs. In a first experiment, the THz response at low lattice temperatures was studied after resonant photoexcitation at the 1*s*-HH exciton line. The THz response is expressed as $\sigma(\omega) = \sigma_1(\omega) + i\omega\varepsilon_0[1 - \varepsilon_1(\omega)]$, where $\sigma_1(\omega)$ measures the absorbed power density and $\varepsilon_1(\omega)$ the inductive out-of-phase response. Just after photoexcitation, as shown in Fig. 5(b), the THz response consists of a strongly asymmetric peak around 1.7 THz in $\Delta\sigma_1$ accompanied by a dispersive dielectric function change $\Delta\varepsilon_1$ at the same frequency. This response corresponds to the formation of a new, low-energy oscillator that is absent in the semiconductor's ground state. The THz conductivity peak can be explained by the lowest energy intra-excitonic transition, i.e. between the 1s → 2p exciton levels, in agreement with known level spacings.

After excitation into the continuum of unbound states, a very different behavior is observed. Fig. 5(c) shows data taken with the sample at room temperature to minimize the influence of excitonic correlations. The THz response then exhibits a pure Drude response of a conducting *e-h* gas. It is characterized by a large low-frequency conductivity $\Delta\sigma_1$ and a purely negative dielectric function change $\Delta\varepsilon_1$. Note in contrast the vanishing low-frequency THz conductivity for the intra-excitonic response in Fig. 5(b), which results from the insulating, charge-neutral nature of the bound *e-h* pairs.

An important advantage of intra-excitonic spectroscopy is its capability to provide an absolute measure of exciton densities. A quantitative intra-excitonic dielectric function $\varepsilon(\omega)$ of an exciton gas in the ground state can be derived by summing up the dipole transitions between the 1*s* level and the higher bound and continuum states. The solid lines in Fig. 5(b) are such calculations, using 2D bound and continuum hydrogenic wavefunctions corrected for Coulomb screening effects due to the finite well width of the quasi-2D system.[42-44] A reduced effective mass $\mu = 0.054\ m_0$ and a dielectric constant $\varepsilon_s = 13.2$ is used for the GaAs quantum well material. The calculation shows that while the peak is due to the 1*s*-2*p* transition, the shoulder stems from transitions into higher bound n*p* levels and the continuum. Within a parabolic band approximation, we can write the "partial oscillator strength sum rule" as

$$\int_0^{W_B} \sigma_1(\omega)d\omega = \frac{\pi}{2}\frac{ne^2}{\mu}. \qquad (6)$$

where *n* is the *e-h* pair density. According to Eq. (6), the intra-band spectral weight up to energies W_B below the inter-band transitions is directly determined by the the *e-h* pair density *n* and reduced mass μ. This renders THz probes an important direct

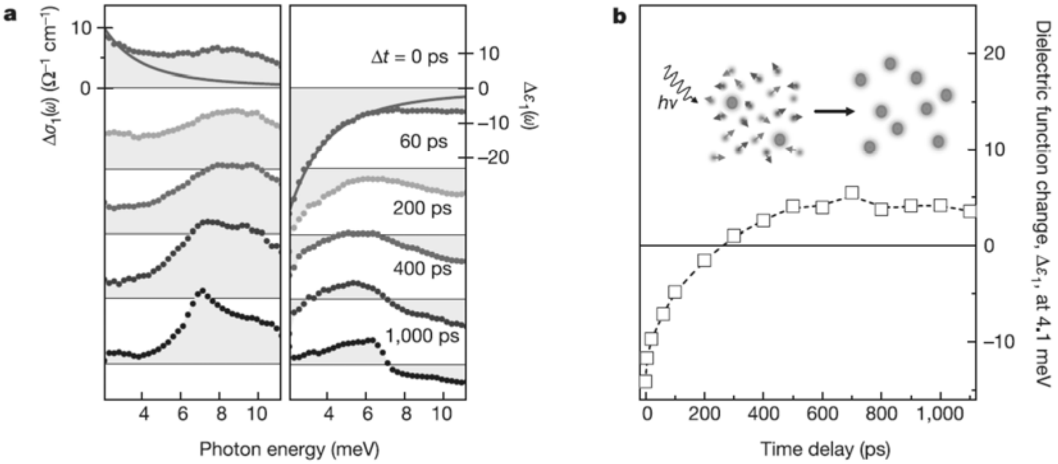

Fig. 6 Exciton formation in GaAs quantum wells at $T = 6$ K, studied via intra-excitonic spectroscopy. **(a)** Induced THz conductivity $\Delta\sigma_1$ and dielectric function change $\Delta\varepsilon_1$ after nonresonant excitation into the continuum, for different pump-probe delays Δt. Solid line at $\Delta t = 0$ ps: Drude model. **(b)** Dynamics of $\Delta\varepsilon_1$ at 1 THz, which illustrates the decay of the Drude-like response of the unbound *e-h* pairs while excitons continue to form. Reprinted with permission from Ref. 37.

gauge of *e-h* pair and exciton densities, in strong contrast to more indirect measures of luminescence or absorption spectroscopy at the band gap.

Optical-pump THz-probe experiments have been employed to investigate the formation and ionization dynamics of excitons.[37] Fig. 6 shows the low-temperature transient THz response after non-resonant excitation above the bandgap. Directly after excitation into the unbound *e-h* continuum ($\Delta t = 0$ ps), the THz response is spectrally broad, with a negative dielectric function change $\Delta\varepsilon_1$ that closely follows a Drude model [solid line, Fig 6(a)]. The system is thus dominated by a conducting gas of unbound *e-h* pairs, as also substantiated by the large low-frequency conductivity. However, the induced conductivity $\Delta\sigma_1$ already at this timepoint deviates significantly from the Drude model, showing a distinct excitonic peak around 8 meV. This peak signifies the quasi-instantaneous appearance of excitonic *e-h* correlations directly after continuum excitation, within the ≈1 ps time-resolution of the experiment. As the system evolves over several 100 ps, the exciton peak increases in spectral weight and sharpens, while the Drude components of the response decay away. This reveals two very different timescales that exist during exciton formation. Acoustic phonon emission can explain the slow scattering of unbound *e-h* pairs into excitons on a 100 ps timescale.[45-47] In contrast, the quasi-instantaneous exciton peak can be explained by a much faster process, such as ultrafast Coulomb interactions in the photoexcited *e-h* gas. The opposite process of exciton ionization at increased lattice temperatures can be studied, where intra-excitonic spectroscopy provides quantitative insight into the dynamics of exciton breakup and into the resulting quasi-

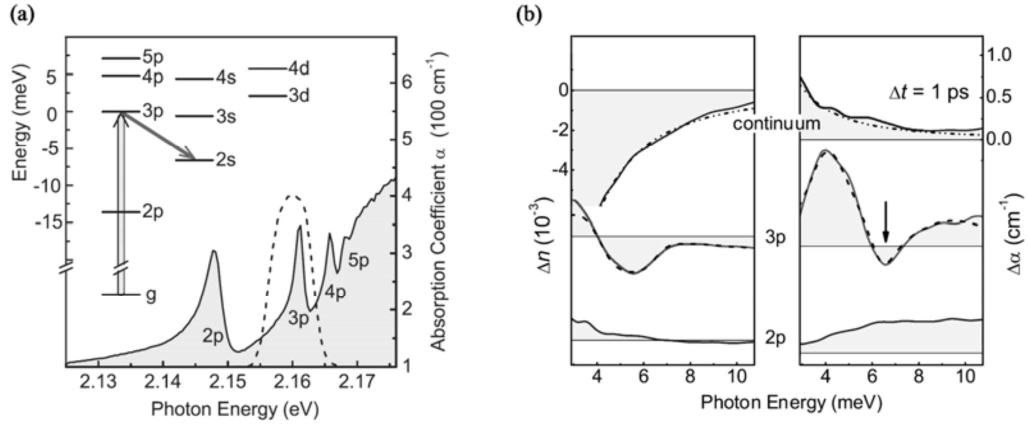

Fig. 7 Stimulated emission from intra-excitonic transitions. **(a)** Visible absorption spectrum of Cu_2O at $T = 6$ K (solid line) and pump spectrum (dashed). Inset: exciton levels and their energy difference to the 3*p* level. **(b)** THz refractive index change Δn (left panel) and induced absorption $\Delta\alpha$ (right panel) 1 ps after continuum, 3*p*, or 2*p* excitation. Arrow indicates 3*p*-2*s* stimulated emission at 6.6 meV. Reprinted figure with permission from Ref. 49, © 2006 by the American Physical Society.

equilibrium mixture of excitons and unbound pairs.[37,44] Further experiments also studied the intra-excitonic response of a high-density exciton gas.[48] Those results show an increasing free carrier fraction as the photoexcitation density is increased, accompanied by a strong renormalization of the 1*s*-2*p* resonance to lower energies.

While the previous experiments have studied intra-excitonic absorption, it was suggested early on to reverse this process in order to induce THz gain from inverted exciton populations.[33] The search for intra-excitonic gain is, however, non-trivial because excitons differ strongly from atomic gases. Excitons interact with phonons and they typically exhibit significant many-body interactions such as phase-space filling, screening, and scattering. Also, in stark contrast to atoms, they are initially photogenerated as coherent polarization waves and possess an often short recombination lifetime. Recent calculations propose to obtain population inversion by exciting higher bound *s*-like excitons and predict a transfer into *p*-like excitons via many-body interactions.[50] A promising candidate for intra-excitonic stimulated THz emission is Cu_2O, which exhibits a particularly well-defined excitonic Rydberg series. These visible lines shown in Fig. 7(a) are due to *p*-like excitons,[51] which makes this an ideal system to search for $p \rightarrow s$ intra-excitonic population inversion. Unlike most semiconductors, photoexcitation of *s*-like excitons in Cu_2O is dipole forbidden because the parity of valence and conduction bands is identical around the Brillouin zone center.[51]

A recent optical-pump THz-probe experiment provides the first demonstration of stimulated emission between internal exciton levels.[49] In that study, a 330-μm thick Cu_2O single crystal was resonantly photoexcited using spectrally-shaped pump pulses around $\lambda \approx 570$ nm. Figure 7(b) shows the THz response at $\Delta t = 1$ ps. Excitation in the continuum leads to a broad Drude response (top curve), while excitation of 2*p* excitons (bottom curve) induces a broad THz absorption that can be explained by intra-excitonic transitions. A strikingly different response occurs after selective 3*p* excitation, as shown in the middle curve of Fig. 7(b): here, a *negative* absorption change at 6.6 meV is observed which is surrounded by absorption at higher and lower photon energies. This negative absorption is explained by $3p \rightarrow 2s$ stimulated THz emission, commensurate with the known level spacing. It should be noted that Cu_2O has no measurable absorption in this range, and that the effect occurs only after resonant 3*p* excitation. While the overall signals are small, the cross section corresponds to a large value of $\sigma \approx 10^{-14}$ cm^2 which motivates further work towards generation of strong stimulated THz emission from excitons.

The material Cu_2O has also been of much interest for experiments that attempt to find Bose-Einstein condensation (BEC) of excitons in semiconductors. Exciton BEC was predicted in 1968 by Keldysh and Kozlov,[52] but its observation has been elusive until now. The small exciton mass pushes the transition temperature upwards into the Kelvin range, about 10^6 times higher than for atoms. Very intriguing effects were observed in coupled quantum wells,[53,54] but Cu_2O remains the longest and most extensively studied candidate material. It is a key contender for BEC because its lowest-energy 1*s* exciton is dipole forbidden and thus has an extremely long lifetime. Due to electron-hole exchange interactions, the 1*s* exciton in Cu_2O is split into the lowest-energy *paraexciton* (singlet, S=0) and a three-fold degenerate *orthoexciton* (triplet, S=1) that lies 12 meV higher in energy, see Fig. 8(a). The paraexciton is optically inactive to all orders, and lifetimes from ≈ 0.1 - 1 ms have been reported. Luminescence experiments provided strongly differing interpretations: an early study suggested evidence for exciton BEC in Cu_2O based on the luminescence lineshape,[55] but the same authors later questioned this[56] and concluded that the densities for BEC may not be reached due to fast exciton-exciton Auger recombination above $n \approx 10^{15}$ cm^{-3}. However, Auger recombination was shown to contradict recent results, and a fast exciton capture into short-lived biexcitons was proposed instead to explain the fast dynamics.[57-59]

Here, intra-excitonic spectroscopy promises new insights due to the lack of optical coupling of the 1*s* exciton in the visible inter-band range. Several intra-excitonic experiments were reported that probe the 1*s*-2*p* transitions in Cu_2O crystals.[38,60-64] Kubouchi *et al.* studied the picosecond dynamics of the intra-excitonic transitions of the lowest energy exciton species in a 170 μm thick Cu_2O single crystal.[38,63,64] As illustrated in Fig. 8(a), the 1*s*-2*p* transitions within the paraexcitons occur at higher photon energies than within the orthoexcitons, due to the different fine structure splittings of the 1*s* versus the 2*p* levels. Orthoexcitons in the 1*s* level are resonantly photogenerated in those experiments by two-photon excitation with a femtosecond

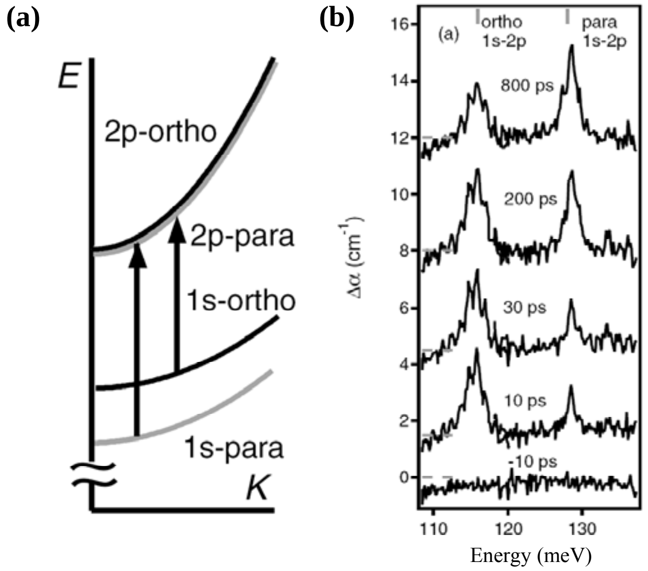

Fig. 8. (a) Schematic level diagram of the lowest energy excitons in Cu_2O, along with intra-excitonic transitions between the 1*s* and 2*p* levels. **(b)** Transient intra-excitonic absorption at 4.2 K for different time delays after two-photon resonant excitation of orthoexcitons with a 1220 nm wavelength pump beam. Reprinted figure with permission from Ref. 38. © 2005 by the American Physical Society.

pulse around 1220 nm wavelength.[38] The resulting absorption changes $\Delta\alpha$ are followed in transmission between 108 and 140 meV photon energy (≈ 26-34 THz) on a ps timescale. As shown in Fig. 8(b), the signals directly evidence a decrease of the orthoexciton density (116 meV peak) accompanied by a concomitant rise of the paraexciton density (129 meV peak) on a 100 ps timescale. This intra-excitonic study therefore shows directly that rapid orthoexciton decay arises from ortho-para exciton *interconversion*. This can be attributed to an electron spin exchange mechanism. Such experiments can provide new insight into the properties of the optically-dark 1*s* excitons, to optimize the conditions under which a possible degenerate excitonic quantum state may be generated. Moreover, calculations predict strong changes of the intra-excitonic spectra when the material undergoes a transition into the BEC state,[39] which strongly motivates further work on intra-excitonic spectroscopy of low-temperature *e-h* gases.

2.4 INTERSUBBAND TRANSITIONS

The quantum confinement of carriers in semiconductor heterostructures leads to a splitting of the conduction and valence bands into subbands. New THz transitions can then occur between these subbands within the conduction band (or valence band) when a quasi-two dimensional carrier plasma is introduced into the structure by photoexcitation, electrical injection, or chemical doping. These *intersubband* transitions represent a totally new character of opto-electonic excitations below the fundamental band gap of a semiconductor, especially when compared to the broad near-infrared interband absorption from the valence to conduction bands.[65,66] A schematic band structure and a typical intersubband absorption line are shown in Fig. 9. Due to the identical sign of the curvature of both subbands, the absorption is concentrated into a small interval of photon energies. Ideally, subbands with identical effective mass would result in a vanishing linewidth except for homogeneous broadening. However, a real semiconductor exhibits a nonparabolic band dispersion: transitions at different in-plane momenta then occur in a finite frequency interval, leading to inhomogeneous broadening. Sample imperfections and Coulomb many-body interactions further complicate intersubband line shapes.

Intersubband transitions can be tailored to occur within a large photon energy range from approximately 1-100 THz via quantum heterostructure engineering. Technical applications of intersubband transitions are abundant, with unipolar quantum well photodetectors and quantum cascade lasers being particularly relevant devices.[67,68] The operating principle of THz and mid-infrared quantum cascade lasers relies directly on controlled engineering of ultrafast processes. Population inversion between subbands can be achieved by optimizing the electron tunneling and relaxation dynamics, and the photonic properties of quantum well and superlattice heterostructures.

Numerous ultrafast THz and mid-infrared studies of intersubband relaxation and dephasing have been reported. Intersubband relaxation and carrier thermalization has been observed in both *n*-type and *p*-type heterostructures, where spectral changes

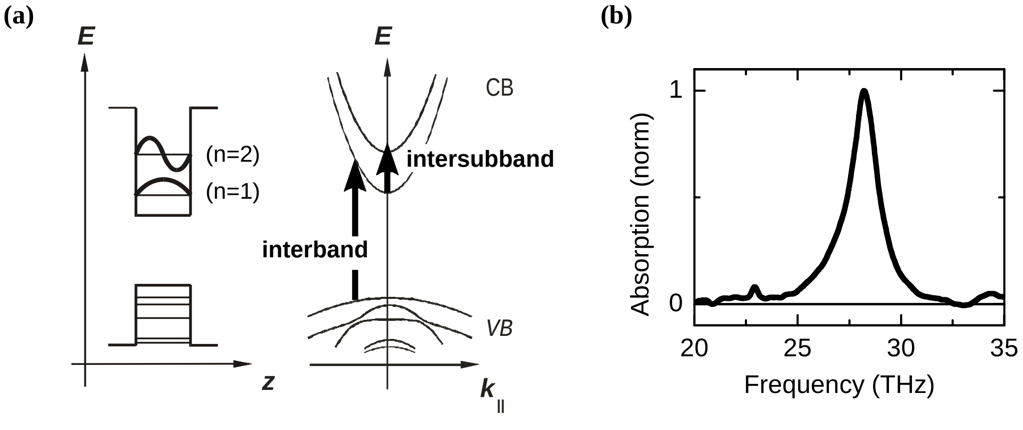

Fig. 9 Intersubband Absorption. (a) Left: spatial variation of the conduction (CB) and valence band (VB) edges in the heterostructure growth direction, and energy extrema of the lowest subbands (horizontal lines). Right: dispersion along the 2D layers and optical transitions. (b) Typical intersubband absorption line, measured from an n-type doped GaAs multiple quantum well structure.

around the intersubband line are sensitive to transient modifications of the carrier distribution function $f(E)$.[69-75] Near-infrared photoexcitation of a coherent superposition of several bands also leads to THz emission, as a measure of intersubband or inter-valence band oscillations.[76-78] This yields information on the decay of intersubband coherence in undoped structures, equivalent to the overall intersubband line shape. Coherent emission was also detected from intersubband plasmons in parabolic quantum wells,[79] and from Bloch oscillations in superlattices that arise from different physics in high THz fields.[80] Separation of homogeneous and inhomogeneous components of intersubband line shapes neccessitates nonlinear experiments, which was realized through mid-infrared femtosecond four-wave-mixing experiments.[81,82] Such time-resolved THz and mid-infrared studies provide insight into energy and phase relaxation times, and into microscopic carrier-carrier and carrier-lattice interactions of interest for fundamental physics and device design.[83]

Combined with high field strengths, coherent THz pulses offer new ways to measure and control coherent polarizations between quantized levels in quantum wells or other nanomaterials. Intense THz fields can lead to the generation of intersubband sidebands on the near-infrared resonances, and to undressing of collective depolarization effects.[84,85] Rabi oscillations occur at the highest field strengths. The experiments of Luo *et al.*, discussed in the following, have provided a vivid example of direct field-resolved measurements in this regime.[86] The experiment is illustrated in Fig. 10(a): an incident coherent THz pulse couples to the (n=1) to (n=2) intersubband transition ($\nu_{IS} \approx 24$ THz) in the mid-infrared spectral range of an *n*-type modulation-doped GaAs multiple-quantum-well structure. The electron density is 5×10^{10} cm^{-2} in each quantum well. A prism geometry enables strong coupling to the intersubband dipole moment oriented perpendicular to the quantum well layers. The incident and re-emitted light fields are characterized in the time-domain via electro-optic sampling using a 10-μm thick ZnTe crystal. Figures 10(b) and (c) show the "incident field" and the re-emitted field for different field strengths. The incident field is determined by use of an inactive undoped sample. The "emitted field" in turn is obtained by subtracting the incident field from the total field transmitted through a doped sample. In the weak-field limit shown in Fig. 10(b), the re-emitted THz field is 180° out of phase from the incident field. This corresponds to *absorption* of light at the intersubband transition: the incident field creates a coherent intersubband polarization, from which a coherent field is emitted (free induction decay) that partially cancels the incident THz pulse. At higher field strengths, Fig. 10(c), the re-emitted field changes drastically: initially it is out of phase, then vanishes and reappears as in-phase with the driving field. Constructive interference with the re-emitted field during the second half of the driving pulse corresponds to *gain* and thus to amplification of the incident field. This is a direct manifestation of Rabi oscillations between the (n=1) and (n=2) subbands. A detailed analysis of the

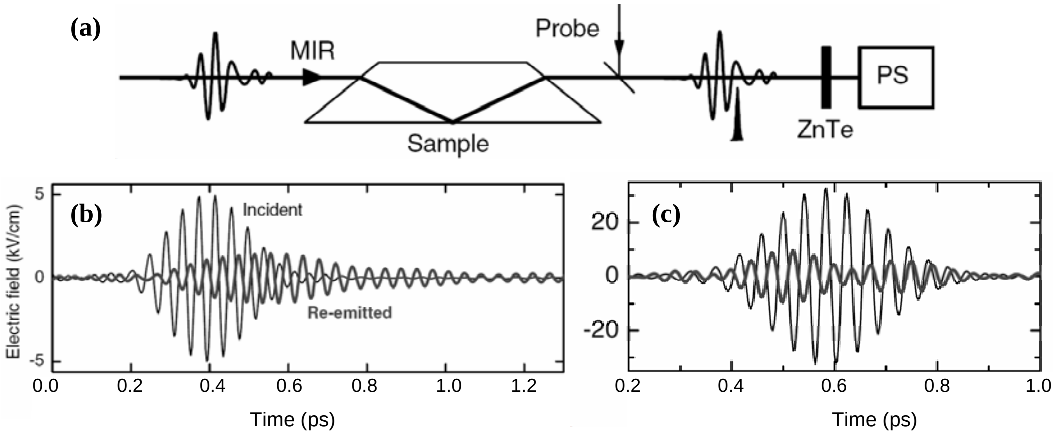

Fig. 10 Rabi oscillations from intersubband transitions in GaAs multiple quantum wells. (a) Experimental scheme. (b),(c) Measured field transients incident (thin line) and re-emitted (thick line) from the sample, for two different THz field amplitudes of 5 kV/cm and 30 kV/cm. Reprinted figure with permission from Ref. 86. © 2004 by the American Physical Society.

data reveals deviations between the simplified two-level Maxwell-Bloch formalism and the measured field traces.[86] This can be explained by a Coulomb-mediated collective coupling between different quantum well layers in the nanostructure.[86-88]

Intersubband coherent control via high-field THz pulses enables new quantum optical experiments in solids, with novel applications e.g. in photonics and quantum information science. Rabi oscillations were also studied on hydrogenic 1*s*-2*p* transitions of donor impurities in GaAs,[89] which serve as a model two-level system for such applications. Gain without inversion from intersubband transitions was recently experimentally observed.[90] This also motivates coherent population transfer experiments to provide maximum control over THz excitations in nanostructures.[91-93]

3. SUPERCONDUCTORS

3.1 OVERVIEW

Far-infrared spectroscopy has played an important role in the characterization of superconductors ever since the BCS phonon-mediated pairing mechanism was proposed and experimentally verified.[94] Mattis and Bardeen described the electrodynamics of superconductors and the opening of a spectroscopic gap $2\Delta_0$ for quasiparticle excitations.[95] In weak-coupling BCS theory, the gap value is given by $2\Delta_0 = 3.5k_BT_C$, with T_C being the transition temperature. The electrodynamics was experimentally confirmed by Glover and Tinkham using far-infrared techniques.[10,96]

Nonequilibrium superconductivity also has a long history starting with tunneling experiments.[97] The formation of Cooper pairs - also called “quasiparticle recombination” - is a fundamental quantum process in a superconductor arising from the pairing of two unbound quasiparticles which are thermally or otherwise excited out of the condensate’s correlated ground state. It was soon realized that pair-breaking by excess phonons complicated matters, as first described by the rate equations of Rothwarf and Taylor.[98] Experimental and theoretical progress continued throughout the 1970’s and 80’s.[99-102] Ultrafast optical spectroscopy of metals blossomed when it was realized that the electron-phonon coupling constant λ could be determined from such experiments.[103-105] For example, this technique was used to measure λ for several conventional BCS superconductors.[106] With the discovery of high-T_C superconductors in the copper-oxides (cuprates), it was realized that all-optical pump-probe spectroscopy could be used for nonequilibrium studies below T_C.[107,108] A limitation in the interpretation of such studies is that they probe the dynamics at visible or near-IR wavelengths, far above the superconducting gap and other intrinsic low-energy excitations.

THz-TDS is a useful experimental tool to study superconductors.[106,109] With optical photoexcitation it provides what, to date, is probably the most insightful experimental approach to interrogate nonequilibrium dynamics in superconductors. Such experiments have the potential to measure quasiparticle interactions that remain hidden in linear spectroscopic measurements. In this section, we first describe linear infrared spectra of superconductors using THz-TDS, with an emphasis on MgB_2 and $YBa_2Cu_3O_7$. This highlights commonalities and differences between conventional and high-T_C superconductors in their THz electrodynamics. Armed with this knowledge, we proceed in the subsequent sections to time-resolved THz studies of nonequilibrium dynamics in the BCS superconductor MgB_2, and in the high-T_C cuprates YBCO and Bi-2212.

3.2 FAR-INFRARED SPECTROSCOPY OF SUPERCONDUCTORS

There is a vast literature on the electrodynamics of superconductors.[1,10] Given these excellent reviews and space limitations we restrict our description to studies of superconductors using THz-TDS. The advantage of THz probes is that they significantly penetrate inside the bulk of the material to provide a contactless probe of low-energy excitations such as the superconducting energy gap and the collective superfluid condensate and quasiparticle response.[110] Early time-domain THz experiments on superconductors concentrated on studying the equilibrium conductivity of conventional metals such as NbN that exhibit an isotropic s-wave superconducting gap,[13] and of high-T_C cuprates[109,111-113] with an anisotropic *d*-wave gap and more complex physics.

In the following, we first illustrate the THz response of a superconductor with a time-domain THz study of MgB_2.[114] As discovered in 2001, this material turns superconducting below $T_C = 39$ K, an unexpectedly high transition temperature for a conventional metallic compound.[115] The THz experiments described below cover the 2-11 meV spectral range, with THz pulses generated and coherently detected using a 250-kHz Ti:sapphire amplifier. Experimental results are shown in Fig. 11, as obtained from a 100-nm thick MgB_2 film. The electric field of THz pulses transmitted through the film is shown in Fig. 11(a). As the material transitions from the normal (dashed) into the superconducting state (solid line), the THz field increases in amplitude and shifts in phase. This field reshaping arises from changes to the complex conductivity $\sigma(\omega)$. The response is obtained via Fourier transformation of time-domain THz signals and by evaluation of standard thin film transmission formulas.[116]

A useful way to analyze the electrodynamic properties of superconductors is to plot the ratio of the conductivity to its normal state value $\sigma_N(\omega)$. This is shown in Fig. 11(b), (c) for the real and imaginary parts, respectively. A strong depletion in the real part $\sigma_1(\omega)/\sigma_N(\omega)$ is evident in Fig. 11(b) as the temperature is decreased below T_C. An absorption onset occurs at ≈ 5 meV, as evident in the data particularly at the lowest temperature, $T = 6$ K. This is the signature of the superconducting gap. The imaginary part $\sigma_2(\omega)/\sigma_N(\omega)$ in Fig. 11(c) shows the buildup of a component in the superconducting state that strongly increases with decreasing frequency. The latter, $1/\omega$–like response is the hallmark of a superconductor: it arises from the purely inductive motion of the superfluid in the electromagnetic THz field. The results were compared to calculations with Mattis-Bardeen theory for BCS superconductors with an isotropic s-wave gap,[95] shown as lines in Figs. 11(b) and (c). This theory is valid in the so-called "dirty limit", which occurs when the superconducting gap $2\Delta_0$ is much smaller than the normal state Drude width $1/\tau$. In this case, absorption sets in for frequencies above the superconducting gap 2Δ, where elastic scattering with rate $1/\tau$ enables momentum conservation during THz absorption.

The Mattis-Bardeen theory faithfully represents both real and imaginary parts of the experimental data. The gap in the real part reflects the fact that, at the lowest temperatures, Cooper pair breaking is only possible for photon energies above $2\Delta_0$. At higher temperatures, the gap value decreases, and thermally-excited quasiparticles exhibit an additional Drude-like response which results in the conductivity $\sigma_1(\omega)$ even below the gap. The temperature dependence of the superfluid response in σ_2, which vanishes at $T_C = 30.5$ K, is equally well reproduced (see Ref. 114). However, this overall agreement is possible only when an artificially small gap value of $2\Delta_0 = 5$ meV is assumed in the calculations. This value is almost a factor of two smaller than the ratio expected from the known T_C even in weak-coupling BCS theory, which predicts $2\Delta_0 = 3.5\ k_B T_C \approx 9$ meV.

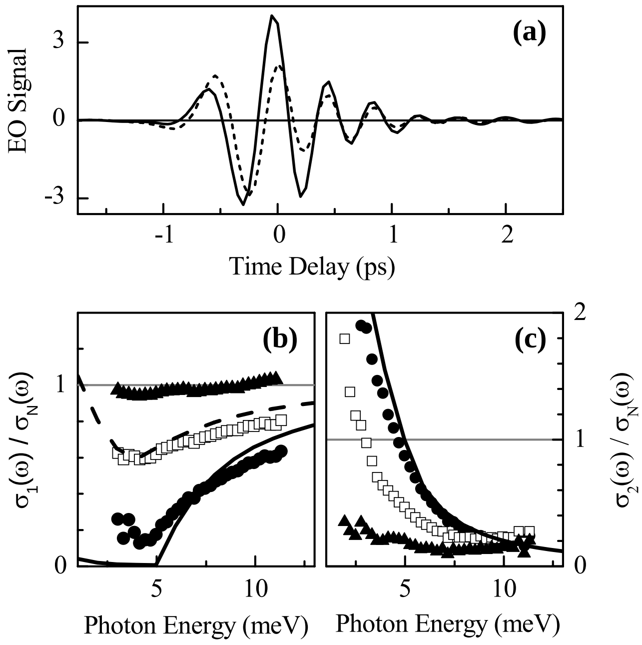

Fig. 11 Terahertz conductivity of a 100-nm thick film of MgB_2. **(a)** Time-resolved THz fields measured in transmission at $T = 6$ K (solid line) and 40 K (dashed line). **(b),(c)** Real part $\sigma_1(\omega)$ and imaginary part $\sigma_2(\omega)$ of conductivity normalized to the normal state (40 K) value $\sigma_N(\omega)$. Data are shown for $T = 6$ K (dots), 24 K (squares), and 30 K (triangles). Mattis-Bardeen calculations for an isotropic s-wave gap of magnitude $2\Delta_0 = 5$ meV, $T_C = 30$ K, and $T = 6$ K are shown as thick solid lines. The dashed line in panel (b) also shows the same calculation for $T = 24$ K.

This persistently small gap size is a fundamental property of MgB_2, which is also seen in numerous other experiments. In contrast to surface sensitive measurements, however, the THz probe penetrates through the bulk of the film and thus confirms the general presence of the small gap. The small gap value is explained by the existence of *two* superconducting gaps, of which the smaller one dominates the optical conductivity.[117-119] First-principle bandstructure calculations confirm this novel physics and indicate that the dominant hole carriers in Boron *p* orbitals are split into two distinct sets of bands with quasi-2D and 3D character. The coupling between these bands leads to MgB_2's novel superconducting state with two gaps but a single T_C.

In contrast to conventional narrow-gap superconductors such as MgB_2, the THz electrodynamics of high-T_C cuprates is quite different.[1,106] Most notably, the superconducting gap has a *d*-wave symmetry and peaks around 30 THz, such that the typical BCS gap structure in $\sigma_1(\omega)$ (Fig. 11) is not observed in the 1-3 THz range. However, as with the BCS superconductors, a strong $1/\omega$ dependence from the inductive condensate response is quite prominent in $\sigma_2(\omega)$ below T_C. A model that describes the electrodynamics of superconductors at frequencies far below the gap is the *two-fluid model*. It is useful to approximate the response of high-T_C cuprates in the range up to ≈ 3 THz. The two fluids in this model refer to thermally-excited quasiparticles and the superconducting condensate. With decreasing temperature, more quasiparticles join the condensate. Thus, the quasiparticle density $n_N(\mathrm{T})$ and the condensate density $n_{SC}(\mathrm{T})$ are temperature dependent. The sum of quasiparticle and condensate densities is constant with temperature: $n_N(T) + n_{SC}(T) = n$ where n is the normal state carrier density above T_C. This can also be written as $X_N(\mathrm{T}) + X_{SC}(\mathrm{T}) = 1$ where $X_N(\mathrm{T}) \equiv n_N(\mathrm{T})/n$ is the quasiparticle fraction and $X_{SC}(T) \equiv n_{SC}(T)/n$ is the condensate fraction. The conductivity for the two-fluid model is given as

$$\sigma(\omega) = \frac{n_N(T)e^2}{m^*}\frac{1}{1/\tau(T) - i\omega} + \frac{n_{SC}(T)e^2}{m^*}\left[\pi\delta(\omega) + \frac{i}{\omega}\right] \qquad (7a)$$

$$= \frac{\varepsilon_0\omega_p^2}{1/\tau(T) - i\omega}X_N(T) + \frac{1}{\mu_0\lambda_L^2(0)}\left[\pi\delta(\omega) + \frac{i}{\omega}\right]X_{SC}(T). \qquad (7b)$$

The first term is just the Drude response with a temperature dependent carrier density and scattering time. The second term describes the condensate response with the first term in brackets being a δ-function at zero frequency that describes the infinite d.c. conductivity of the superconducting condensate. The second term in brackets is a purely imaginary, inductive response (obtained by letting $\tau \to \infty$ in the Drude model). We can thus see that upon condensation of quasiparticles into the superfluid, spectral weight is transferred from the Drude peak to the zero frequency superconducting peak. In Eqn. (7b), the condensate portion is rewritten in terms of the London penetration depth

$$\lambda_L^2(0) = \frac{m^*}{\mu_0 n e^2}, \qquad (8)$$

which describes how far a DC magnetic field penetrates into the superconductor at zero temperature. The above equations highlight an important aspect about the electrodynamics of superconductors: from a simultaneous measurement of $\sigma_1(\omega)$ and $\sigma_2(\omega)$, the quasiparticle and condensate fractions can be quantitatively determined. The temperature dependence of these fractions then can provide essential information about the superconducting state, to distinguish e.g. isotropic *s*-wave from anisotropic *d*-wave gap symmetries.[106]

Figure 12 shows a calculation using the two-fluid model for various values of X_N and X_{SC} (keeping $X_N + X_{SC} = 1$). For the calculations, $\tau = 150$ fs, $n = 10^{19}$ cm^{-3}, and $m^* = m_0$ giving $\sigma_{DC} = 10^4\ \Omega^{-1}\mathrm{cm}^{-1}$ for $X_N = 1$. The real part $\sigma_1(\omega)$ is shown as a solid line, the total $\sigma_2(\omega)$ is plotted as a dashed line, and the Drude contribution to $\sigma_2(\omega)$ is plotted as a dotted line. A pure Drude response results for $X_{SC} = 0$, see Fig. 12(a). With $X_{SC} = 0.2$, a clear $1/\omega$ dependence is evident, although the relative Drude contribution to $\sigma_2(\omega)$ is still quite large but becomes much smaller at $X_{SC} = 0.4$. Finally, for $X_{SC} = 1$ as shown in Fig. 12(d), the response at THz frequencies entirely arises from the superconducting condensate.

Of course this idealized situation is not practically realized, though as Fig. 13 reveals, it provides a good starting point. Specifically, Fig. 13 shows the results of THz-TDS measurements on a near optimally doped film of $YBa_2Cu_3O_7$ ($T_C = 89$ K) expitaxially grown on <100> MgO using pulsed laser deposition. Fig. 13(a) shows $\sigma_2(\omega)$ at T = 60 K while panel (b) shows $\sigma_2(\omega)$ at 95K. The insets show the corresponding real part $\sigma_1(\omega)$. The thick solid lines are the experimental data and the dashed lines are fits using the two-fluid model. In (a), the Drude contribution to $\sigma_2(\omega)$ is plotted as a thin solid line with the condensate fraction plotted as a thin dotted line. The two-fluid model provides a reasonable fit to the data. In Fig 13(c), $X_N(T)$ and $X_{SC}(T)$ are shown as extracted from fits to the experimental data. The relation $X_N(T) + X_{SC}(T) = 1$ is seen to be accurate to within 10%. At the lowest temperature measured, $X_N(T) = 0.1$ which is still a substantial quasiparticle fraction. In Fig. 13(d), τ is plotted as a function of temperature. Below T_C, there is a dramatic increase in the scattering time until ~50 K where it saturates at 400 fs due to impurity scattering. This increase in τ results in a substantial narrowing of the Drude peak, see inset to Fig. 13(a).

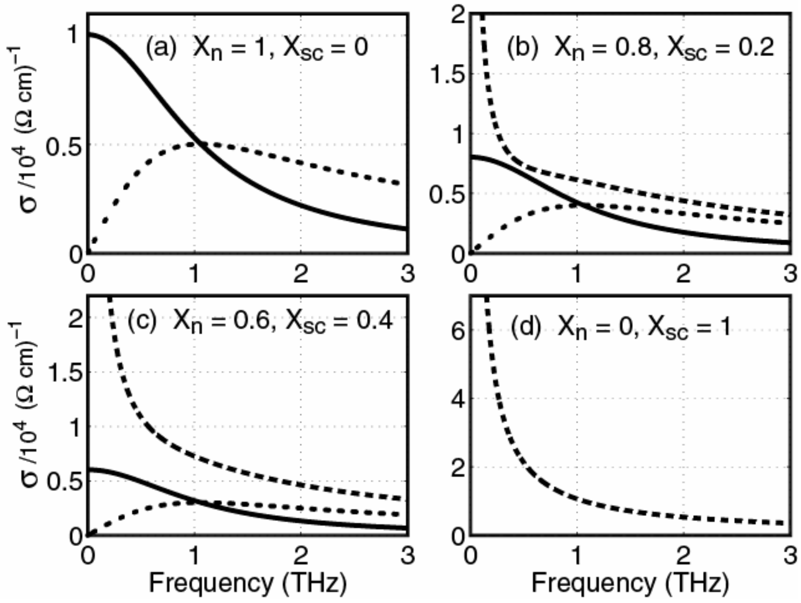

Fig. 12 Model calculation using the two-fluid model for different values of the quasiparticle and condensate carrier fractions.

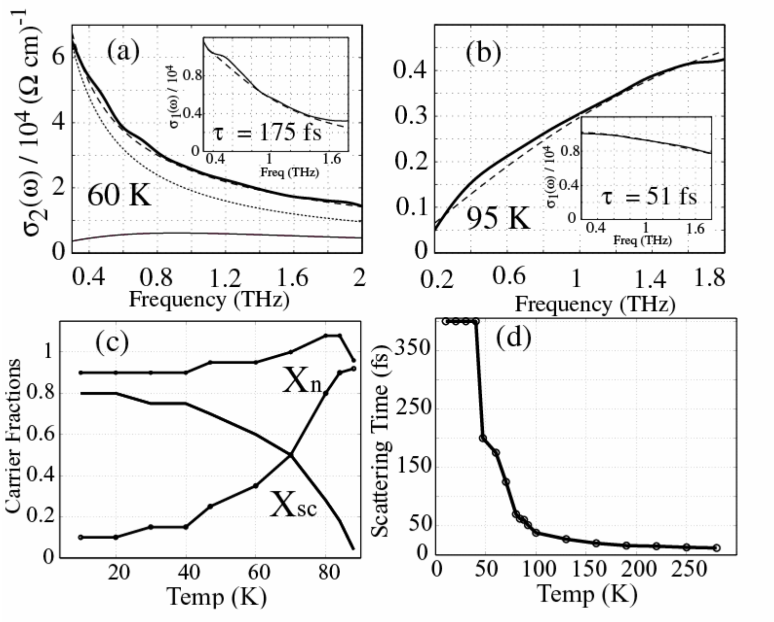

Fig. 13 THz-TDS measurements on $YBa_2Cu_3O_7$ with two-fluid model fits, as explained in the text.

However, in even the best films τ is still much shorter when compared to the highest quality single crystals where τ is so long that the Drude peak lies at microwaves frequencies.[120]

Time-domain THz spectroscopy was also used to study the conductivity in another important cuprate, $Bi_2Sr_2CaCu_2O_{8+\delta}$ (Bi-2212). In this material, about 30% of the spectral weight resides in an additional component that follows the temperature dependence of the superfluid but exhibits a finite scattering width 1/τ (Ref. 121). This has been associated with static fluctuations of the superfluid due to real-space electronic inhomogeneity in Bi-2212, i.e. can be described as a disordered condensate response. Furthermore, THz-TDS experiments can be carried out on underdoped cuprates, which are known to exhibit a puzzling "pseudogap" phenomenon that appears in numerous spectroscopies and persists to temperatures well above T_C. Among various explanations, the pseudogap has been ascribed to a transient phase-coherence due to short-lived remnants of the superfluid above T_C. Here, THz-TDS experiments on underdoped Bi-2212 films have revealed that while such coherence indeed persists above T_C, it cannot be the main source of the pseudogap because it vanishes already well below the pseudogap temperature.[122]

Despite the subtleties of the cuprate properties, the two-fluid model (Eqns. 7 and Fig. 12) is still a reasonable starting point for understanding their THz response well below the gap, and accordingly for insight into the nonequilibrium dynamics. Anticipating the dynamic experiments to be described later, the model suggests how we can fruitfully apply optical-pump THz-probe spectroscopy to superconductors. A short near-infrared pulse breaks Cooper pairs, thereby reducing the condensate fraction and increasing the quasiparticle fraction. Subsequently, the excess photoexcited quasiparticles will recombine to the condensate. This process can be monitored in exquisite detail using THz pulses, allowing for the simultaneous measurement of the dynamical evolution of quasiparticle and condensate densities, i.e. of their time-dependent change $\Delta n_N(t)$ and $\Delta n_{SC}(t)$.

3.3 QUASIPARTICLE DYNAMICS IN CONVENTIONAL SUPERCONDUCTORS

The basic properties of MgB_2 and the electrodynamic response as measured using THz-TDS have been discussed above. In the following, we describe the results of measurements using optical-pump THz-probe spectroscopy on 100-nm films of MgB_2 deposited on sapphire ($T_C = 34$ K).[123,124] In these experiments, 100 fs pulses with a center wavelength of 800 nm were employed to photoexcite the sample at fluences sufficiently low (0.1 – 5 μJ/cm^2) such that the condensate was perturbed without driving the sample above T_C.

In Fig. 14(a), the imaginary conductivity is plotted as a function of frequency at various delays with respect to the photoexcitation pulse. The initial temperature is 7 K and the excitation fluence is moderately high at 3 μJ/cm^2. At Δt = -5 ps, the $1/\omega$ condensate response dominates. At 3 ps the condensate response is dramatically reduced and even more so at 10 ps. By 300 ps, the condensate has still not fully recovered. Interestingly, it takes some time (≈ 10 ps) for the pair-breaking (i.e. reduction in condensate density) to finish. This is shown more clearly in Fig. 14(b) where the dynamics of $\sigma_1(\omega)$ and $\sigma_2(\omega)$ at 0.8 THz are plotted as a function of time. As the condensate response decreases, a corresponding increase in the quasiparticle density is observed in $\sigma_1(\omega)$. This is followed by a much longer recovery time as quasiparticles rejoin the condensate. The condensate recovery time is plotted in Fig. 14(c) and shows a pronounced temperature dependence peaking near T_C. Finally, in Fig. 14(d) the pair breaking dynamics are plotted for various fluences. With increasing fluence, the pair breaking time decreases.

The observed pair-breaking and pair-recovery dynamics in MgB_2 can be understood using the phenomenological Rothwarf-Taylor model.[98] This model consists of two coupled rate equations describing the temporal evolution of the density of excess quasiparticles and phonons injected into a superconductor. The Rothwarf-Taylor equations are written as

$$\frac{dn}{dt} = \beta N - Rn^2 - 2Rnn_T \tag{9a}$$

$$\frac{dN}{dt} = \frac{1}{2}[Rn^2 - \beta N] - \frac{(N - N_0)}{\tau_P}. \tag{9b}$$

Here, n is the excess quasiparticle density, n_T is the thermal quasiparticle density, N is the excess density of phonons with energies greater than 2Δ, R is the bare quasiparticle recombination rate, β is the rate of pair-breaking by ($>2\Delta$) phonons, and τ_P describes the relaxation time of the phonons either by anharmonic decay to phonons with energies $< 2\Delta$ or through phonon escape from the sample (e.g into the substrate). As Eqn. 9a reveals, in the limit of small n_T, the recombination of quasiparticles is a bimolecular process (hence the n^2 term) requiring, as expected, two quasiparticles to form one Cooper pair. However, the direct determination of R is made difficult as it can be masked by excess 2Δ phonons breaking additional Cooper pairs (e.g. the βN term). Thus, in many measurements, it is actually the phonon decay τ_p that is measured which has been termed the phonon bottleneck.

The phonon bottleneck is clearly observed in the condensate recovery dynamics of MgB_2 and Pb superconductors.[125] In MgB_2 the recovery time is largely independent of fluence, see Fig. 14(c), in contrast to bimolecular recombination kinetics. In MgB_2, Pb, and likely all conventional superconductors, the condensate recovery is governed by the decay of acoustic phonons which, as described above, could be due either to

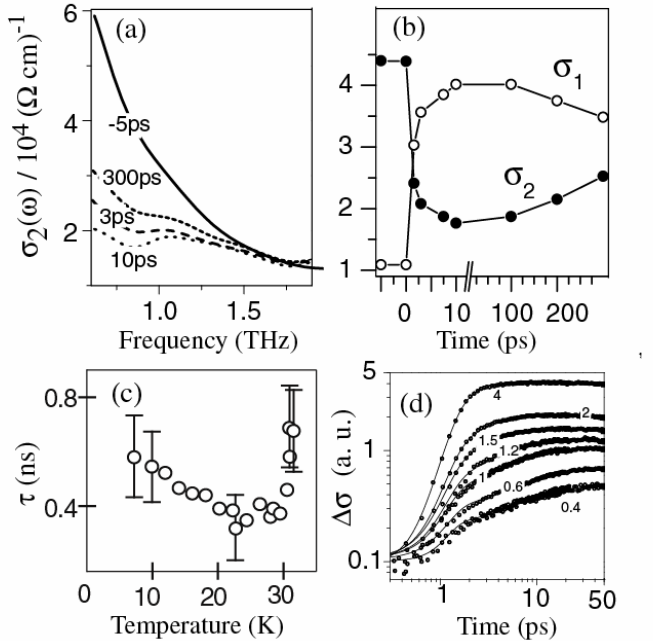

Fig. 14 Optical-pump THz-probe spectroscopy of MgB_2. **(a)** Dynamics of the imaginary conductivity related to the condensate density at T = 7 K. **(b)** Conductivity dynamics at 0.8 THz, for $T = 7$ K. **(c)** Condensate recovery time. **(d)** Initial change in the conductivity related to pair-breaking dynamics at various fluences (in μJ/cm^2).

anharmonic decay or phonon escape from the probe volume. In MgB_2, no change in τ_P was observed as a function of film thickness indicating that phonon escape is not important and the condensate recovery is therefore determined by anharmonic decay processes. This assignment of the recovery is further supported by the observed temperature dependence near T_C showing that $\tau_p \propto 1/\Delta(T)$. This $1/\Delta(T)$ dependence occurs because the superconducting gap decreases in magnitude with increasing temperature. This results, for the same photoexcitation fluence, in a larger density of phonons with energies in excess of 2Δ yielding an increased condensate recovery time.

The early-time pair-breaking dynamics in Fig. 14(d) are somewhat surprising, since after excitation with a 100 fs pulse the reduction in condensate density continues for ≈10 ps. This is in contrast with Pb where the pair-breaking dynamics are complete in ≈1 ps.[126] An understanding of this delayed pair-breaking dynamics can be obtained from the Rothwarf-Taylor equations. In the limit of small n_T and neglecting the term with τ_p (which is reasonable since the condensate recovery timescale is much longer than the initial pair-breaking dynamics) it can be shown that

$$n(t) = \frac{\beta}{R}\left[-\frac{1}{4} - \frac{1}{2\tau} + \frac{1}{\tau}\frac{1}{1-K\exp(-t\beta/\tau)} \right] \tag{10a}$$

$$K = \frac{\frac{\tau}{2}\left(\frac{4Rn_0}{\beta}+1\right)-1}{\frac{\tau}{2}\left(\frac{4Rn_0}{\beta}+1\right)+1} \quad ; \quad \frac{1}{\tau} = \sqrt{\frac{1}{4}+\frac{2R}{\beta}(n_0+2N_0)} \tag{10b}$$

where n_0 and N_0 are, respectively, the initial excess quasiparticle and phonon densities and the timescale of the initial dynamics is given by τ (see Ref. 123). Of particular importance is the dimensionless parameter K which describes three distinct regimes for the pair-breaking dynamics, as manifested in the last term of Eqn. (10a). For $K = 0$ the quasiparticles and phonons are in quasi-equilibrium at an elevated temperature. For this case the initial pair-breaking dynamics would show a step-like dependence at $t = 0$. The regime $0 < K \leq 1$ corresponds to the situation when the density of excess quasiparticles is larger than the quasi-equilibrium ($K = 0$) situation while $-1 \leq K < 0$ corresponds to the situation where the excess density of >2Δ phonons is greater than for $K = 0$. The dynamical signature for this regime is a pronounced risetime and appears to explain the pair-breaking dynamics in MgB_2 in Fig. 14(d). That is, a significant fraction of the energy in the photoexcited quasiparticle distribution is initially transferred to high-energy phonons which subsequently break additional Cooper pairs prior to condensate recovery. This contrasts with a scenario where the photoexcited quasiparticles reach quasi-equilibrium through direct pair-breaking in an avalanche-like process not involving phonons. Fits to the risetime dynamics at various fluences [solid lines in Fig. 14(d)] using Eqns. 10a and 10b permitted a determination of the phonon pair-breaking and bare quasiparticle recombination rates,[123] yielding β^{-1} = 15 ± 2 ps and R = 100 ± 30 unit cell/ps respectively.

3.4 QUASIPARTICLE DYNAMICS IN HIGH-T_C SUPERCONDUCTORS

Knowledge of quasiparticle interactions is particularly relevant for the high-T_C cuprate superconductors, where the mechanism for charge pairing at temperatures up to ≈ 100 K remains unresolved.[127] These materials show a complex phase diagram as a function of chemical doping: with increased density of hole carriers in the Cu_2O planes they transition from an insulating antiferromagnetic state, via a non-Fermi liquid state that shows superconductivity at relatively small T_C ("underdoped") to the state with highest T_C ("optimally doped"). As the doping is further increased, the materials show Fermi liquid properties and a progressively smaller T_C until they are no longer superconducting. The quest to understand the complex quasiparticle properties and interactions in cuprates has inspired numerous experiments that employ visible or near-IR fs pulses to observe optical reflectivity changes at $E \approx 1$-2 eV probe energy.[108,128-130] However, it should be understood that this energy scale far exceeds the fundamental excitations of a superconductor, such as the THz gap and collective quasiparticle and Cooper pair response discussed earlier. Ultrafast THz studies of superconductors, in contrast, can provide a direct measure of quasiparticle and Cooper pair dynamics, but have remained scarce. In the following, we discuss these first THz studies of high-T_C superconductor ultrafast dynamics.

From a simple extrapolation of the dynamics on conventional superconductors one might expect similar dynamics on the high-Tc cuprates. For example, near T_C it was shown that for conventional superconductors the condensate recovery time is proportional to $1/\Delta(T)$. This suggests that the condensate recovery in the cuprates might follow a similar trend, albeit with a shorter lifetime given the larger gaps in these materials. While such behavior is in fact observed and there are similarities between these two classes of superconductors, there are also important differences in the nonequilibrium dynamics (described below) which likely originate from their vastly different microscopic properties. The major microscopic differences are that in the cuprates *(i)* superconductivity is obtained through chemical doping of Mott-Hubbard insulators, *(ii)* superconductivity is thought to occur in two-dimensional CuO_2 planes, *(iii)* the superconducting order parameter has d-wave symmetry resulting in nodes in the superconducting gap (along k_X=k_Y), and *(iv)* there is the distinct possibility that the boson mediating pairing is not a phonon but some other excitation such as antiferromagnetic spin fluctuations. The hope is that optical-pump THz-probe and time-resolved mid-infrared studies can provide insight into the

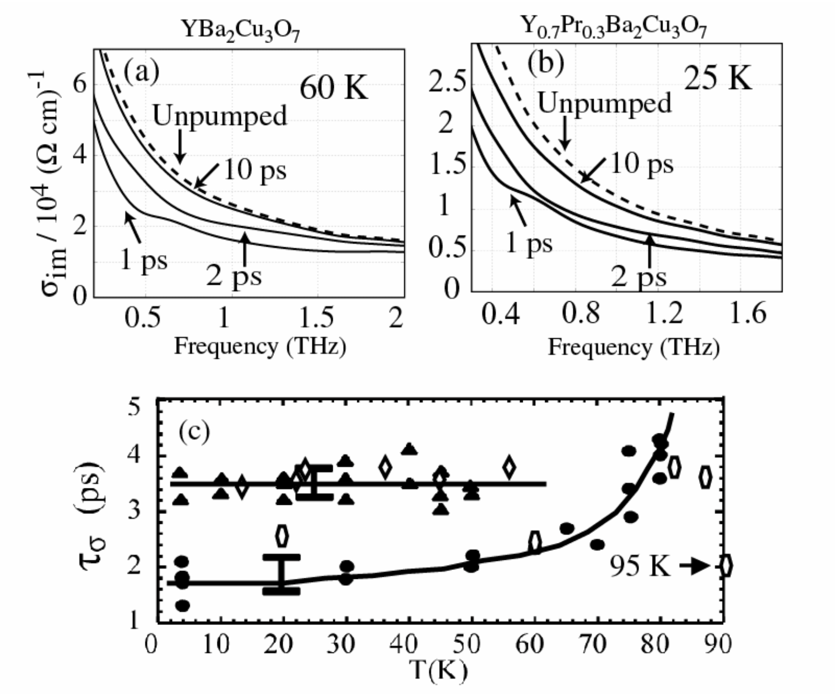

Fig. 15 Condensate dynamics on **(a)** $YBa_2Cu_3O_7$ and **(b)** $Y_{0.7}Pr_{0.3}Ba_2Cu_3O_7$. **(c)** Summary of lifetimes measured on near-optimally doped and underdoped films – the lines are to guide the eye. Triangles: $YBa_2Cu_3O_{6.5}$, diamonds: $Y_{0.7}Pr_{0.3}Ba_2Cu_3O_7$. Closed and open circles: two different $YBa_2Cu_3O_7$ films taken at different fluences.

properties of the cuprates through, for example, extracting the quasiparticle recombination rate or unmasking other interactions that are hidden in various time-integrated spectroscopies.

We will briefly describe the first optical-pump THz-probe experiments which were performed on near-optimally doped and underdoped samples of yttrium-barium-copper-oxide.[131,132] The measurements were made on the same epitaxial films in Fig. 13 and others grown under similar conditions including $YBa_2Cu_3O_{7-\delta}$ with T_C = 89 K (50K) for $\delta = 0$ (0.5) and $Y_{0.7}Pr_{0.3}Ba_2Cu_3O_7$ with T_C = 0.5. The Pr compounds provide an alternate approach to achieve underdoping which is easier than controlling the oxygen stoichiometry. Figure 15(a) shows $\sigma_2(\omega)$ as a function of frequency at various delays following photoexcitation for $YBa_2Cu_3O_7$ at 60 K while Fig. 15(b) shows the dynamics for $Y_{0.7}Pr_{0.3}Ba_2Cu_3O_7$ at 25 K. In both cases, there is a rapid decrease in the condensate fraction followed by a fast, picosecond recovery. The condensate recovery is nearly complete by 10 ps, in dramatic contrast to conventional superconductors.

The extracted lifetimes of the conductivity dynamics, and thus the condensate recovery time, are shown in Fig. 15(c) for all of the samples investigated. In the optimally doped films (closed and open circles) the condensate recovery is approximately 1.7 ps and increases near T_C, consistent with a decrease in the superconducting gap. Above T_C at 95 K, the lifetime has decreased to 2 ps and is likely a measure of electron-phonon equilibration in the normal state. Furthermore, the lifetime is independent of fluence indicative of the absence of bimolecular kinetics although this was not pursued in detail in this work.[131,132] In contrast, for the underdoped films [triangles and diamonds in Fig. 15(c)] the lifetime was constant at ≈3 ps even above T_C. The constant lifetime as a function of temperature is suggestive of a pseudogap. These results revealed that it is possible to sensitively probe the condensate dynamics in the cuprates using optical-pump THz-probe spectroscopy.

A comprehensive study of the transient picosecond THz conductivity changes after ultrafast optical excitation in a different superconductor, $Bi_2Sr_2CaCu_2O_{8+\delta}$ (Bi-2212), has recently been reported.[133] The pump-induced change $\Delta\sigma(\omega)$ of the CuO_2-plane THz conductivity was measured in 62-nm thick optimally doped Bi-2212 films with a transition temperature $T_C \approx 88$ K. As in YBCO, in the superconducting state a $1/\omega$ component dominates the imaginary part of conductivity $\sigma_2(\omega)$ at low frequencies, which provides a direct measure of the condensate density. Figure 16(a) and (b) shows the conductivity change observed directly after photoexcitation. The imaginary part displays a strong decrease, $\Delta\sigma_2 < 0$, due to the depletion of the condensate via interactions with the photoexcited carriers. This superfluid spectral weight is transferred to the quasiparticles, as shown by the broad increase of σ_1. The photoinduced conductivity changes recover on a ps timescale. The changes are well reproduced with the two-fluid model [solid lines in Fig. 16(a),(b)] where the total spectral weight is conserved, or $(e^2/m^*)\,\Delta n_{SC} = -(e^2/m^*)\,\Delta n_N$.

A central result of the Bi-2212 experiments relates to the temporal shape of the relaxation dynamics. Figure 16(c) displays the dynamics of the superfluid density in $\Delta\sigma_2$. Clearly, the decay is non-exponential, which is seen by comparison with the single-exponential model curve (solid line). Figure 16(d) shows the same data on a "reciprocal" scale, i.e. it is plotted $1/\Delta\sigma_2$ versus linear delay time. The decay in Fig. 16(d) shows a strikingly simple linear time dependence

$$\frac{1}{\Delta\sigma_2(t)} = \frac{1}{\Delta\sigma_2(0)} + r \cdot t \,. \tag{11}$$

This linear time dependence plotted on a reciprocal scale is a benchmark for *bimolecular* kinetics. By taking the time derivative of Eq. (11), and taking into account the proportionality $\Delta\sigma_2 \propto \Delta n_{SC} \propto \Delta n_N$ (confirmed by the two-fluid fits at each time delay) we obtain directly $d/dt\,\Delta n_N = -R\,(\Delta n_N)^2$. A natural explanation of this bimolecular kinetics is the pairwise interaction of quasiparticles as they recombine into Cooper pairs. Further evidence for the bimolecular recombination

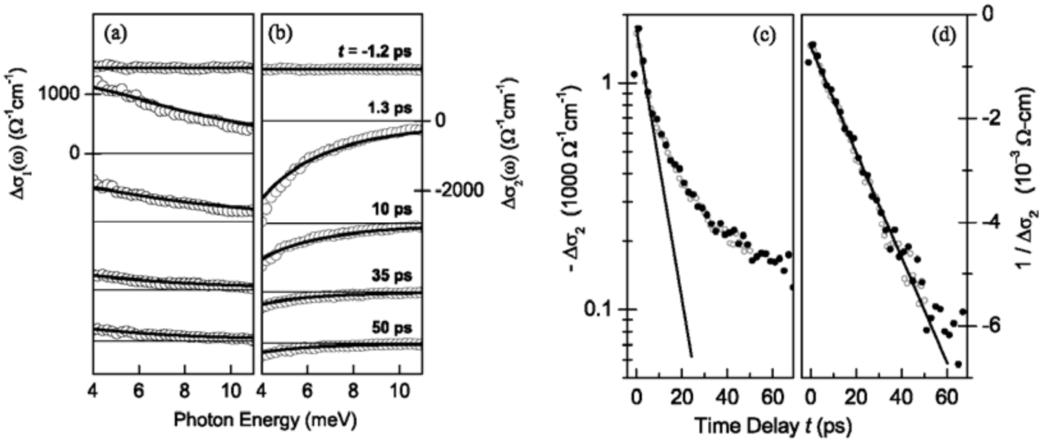

Fig. 16 Dynamics of Cooper Pair formation observed via optical-pump THz-probe spectroscopy of the high-T_C superconductor Bi-2212. The results are for $T = 6$ K lattice temperature and 0.7 μJ/cm^2 fluence of the near-IR excitation pulses. **(a),(b)** Induced changes of the real and imaginary parts of the THz conductivity (circles) for different pump-probe delays *t*. Thick lines: two-fluid model. **(c)** Conductivity dynamics around 5.5 meV probe energy (symbols) plotted on a logarithmic scale. **(d)** The same data as in panel (c), but plotted as $1/\Delta\sigma_2$. The linear decay on this reciprocal scale reveals a bimolecular kinetics of condensate recovery. Solid lines are guides to the eye. Reprinted figure with permission from Ref. 133. © 2005 by the American Physical Society.

picture is obtained from the very strong density and temperature dependence, which is fully explained by the bi-molecular rate equation as discussed in detail in Ref. 133. It has been conjectured that the origin of the fast bimolecular decays in Bi-2212 may be linked to quasiparticle recombination from the anti-nodes of the anisotropic *d*-wave superconducting gap through emission of short-lived high-energy phonons or spin waves.[133] Unlike YBCO, scanning probe microscopies have shown that Bi-2212 exhibits a nanoscale electronic inhomogeneity,[134] which may further relax momentum restrictions for quasiparticle scattering. This may also explain the differences in the dynamics between YBCO and Bi-2212.

While the above studies on cuprates probed changes in the collective charge motion of quasiparticles and Cooper pairs, they do not probe the superconducting gap. For high-T_C superconductors, signatures of this gap occur at higher frequencies around $10-50$ THz ($\approx 40-200$ meV). They are of fundamental significance. Among the longest-standing puzzles of the cuprates is the *pseudogap,* a depression in the electronic density of states.[17,135] It mimics the superconducting gap in energy but appears already at temperatures T^* much higher than T_C. It is widely believed that understanding the correlations that lead to the emergence of this pseudogap will also help clarify the mechanism of superconductivity in the cuprates. Since the pseudogap and superconducting gap are similar in energy, it is difficult to separate them in time-integrated linear spectra. Below, we discuss a first ultrafast study that probes changes in the gap region, enabling separation of components along the temporal degree of freedom.[136] Optimally-doped and underdoped thin films of YBCO (with T_C = 88 and 68 K, respectively) were excited at 1.6 eV with a 2-MHz repetition-rate cavity-dumped Ti:sapphire laser. Terahertz probe pulses spanning the ultrabroadband range from ≈ 14 - 43 THz with 150 fs pulse duration were generated in a novel GaSe-based technique[25] and were employed to detect transient reflectivity changes around the YBCO gap.

As shown in Fig. 17(a), optimally-doped YBCO at low temperatures exhibits a sub-ps reflectivity increase at 21.8 THz probe frequency (90 meV), followed by a decay on a ≈ 5 ps timescale. The amplitude $\Delta R/R$ of this change slowly decreases as the sample temperature is raised, while above T_C it changes into a very fast relaxation dynamics with opposite sign. This difference between the behavior below and above T_C is further corroborated by the spectral response shown in Figs. 17(b) and (c). Below T_C, the induced reflectivity change in Fig. 17(b) shows a strong oscillatory structure. It happens to follow exactly the spectral changes in the stationary

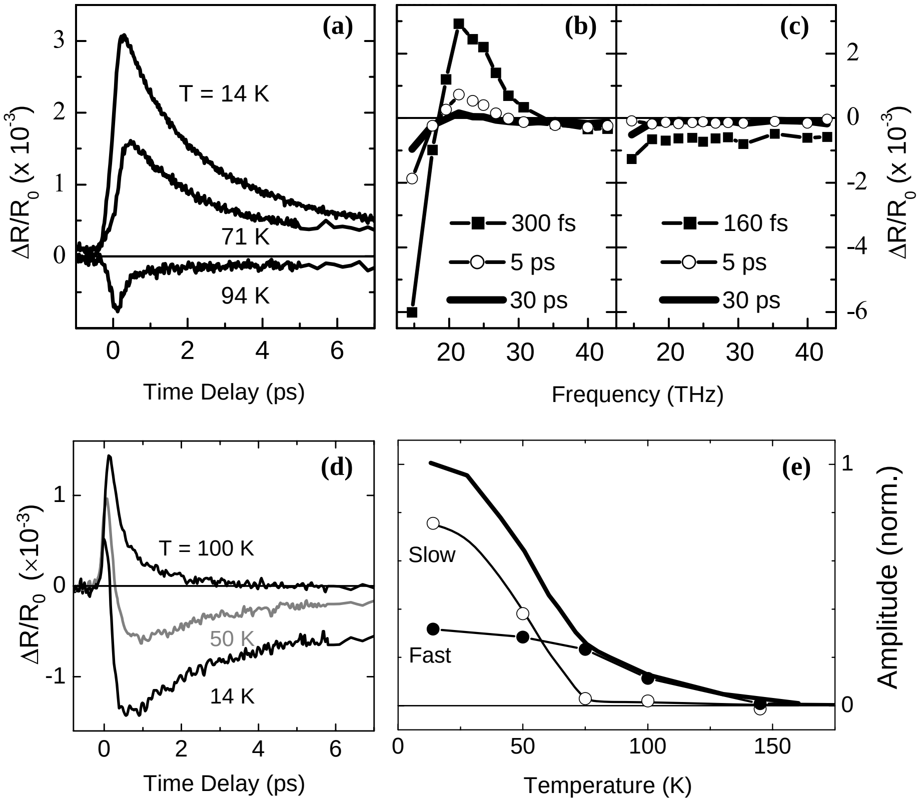

Fig. 17 (a) Transient change of the reflectivity at 21.8 THz in optimally-doped YBCO after near-infrared excitation, for different lattice temperatures T as indicated. **(b),(c)** Spectra of the reflectivity change $\Delta R/R_0$ at different pump-probe time delays for (b) T = 14 K and (c) T = 94 K. **(d)** Dynamics in underdoped YBCO probed at 35 THz, for different temperatures. **(e)** Amplitudes of the fast and slow components (symbols) and the sum total (solid line) of the dynamics in underdoped YBCO.

reflectivity as the sample temperature is lowered from above T_C into the superconducting state (see Refs. 137,138). Hence, below T_C the experiment directly shows the sub-ps reduction of the superconducting gap followed by its re-formation on a 5 ps timescale, in agreement with the timescales of condensate depletion and reformation observed in the 1-3 THz spectral range.[131,133] In contrast, the much faster dynamics and featureless spectra above T_C [Fig. 17(c)] can be attributed to the cooling of a hot carrier distribution analogous to dynamics in metals.[139]

The mid-infrared dynamics in underdoped YBCO show a markedly different dynamics. As seen in Fig. 17(d) for 35 THz probe frequency, the reflectivity change below $T_C = 68$ K cannot be explained by a single decaying component. Rather, it is described by two components: a "fast" reflectivity increase and decay, and a slower ≈ 5 ps constituent which follows the superconducting gap dynamics of optimally-doped YBCO. A more detailed analysis across all probe frequencies showed that both components show a similar (but not identical) spectral shape that corresponds to changes of a conductivity gap around 100 meV. It also provides the temperature dependence of the amplitudes, Fig. 17(e). The "slow" component vanishes at T_C, as in the optimally doped sample – it is a signature of the superconducting gap dynamics due to breakup and re-formation of Cooper pairs. In contrast, the fast ≈ 700 fs component persists up to the pseudogap temperature $T^* > T_C$ ($T^* \approx 160$ K in this sample), and results from ultrafast excitation of a second kind of correlated carriers that lie at the origin of the pseudogap phenomenon. The latter may be due to pre-formed pairs or antiferromagnetic correlations.[135] Thus, the femtosecond study provides a separation of different components of the ≈ 30 THz conductivity gap, which remain hidden in linear spectra. The temperature dependence of the transient signal amplitudes also closely follow the strength of an important, 41-meV antiferromagnetic resonance in cuprates, which supports theories where spin fluctuations couple strongly to the carriers.[136]

The experiments discussed above show the detailed insight into the dynamics of superconductors obtained by employing THz pulses as probes of the fundamental charge excitations. They motivate further work on a larger range of materials to elucidate the differences or similarities in the pseudogap correlations or quasiparticle recombination kinetics. Moreover, almost all previous time-resolved studies of superconductors have employed photoexcitation in the 1-2 eV range. This leads to a cascade of scattering processes as quasiparticles relax to the low energy states, resulting in a fairly indirect and uncontrolled way to break Cooper pairs. We can envision that in the future resonant excitation of superconductors with intense THz pulses at the gap energy $2\Delta_0$ will be possible, leading to direct control of (and consequently even more detailed insight into) the nonequilibrium state of superconductors.

4. HALF-METALLIC METALS: MANGANITES AND PYROCHLORES

4.1 OVERVIEW

Manganite perovskites such as $R_{1-x}D_xMnO_3$ (where R = La, Nd and D = Ca, Sr) and related compounds are similar to the cuprates in that their parent materials (e.g. $LaMnO_3$) are Mott-Hubbard insulators. As a function of doping, fascinating states occur ranging from charge-ordered insulator to ferromagnetic metal phases. The most studied materials of this class during the past decade are the optimally-doped manganites around $x \approx 0.3$, which includes $La_{0.7}Ca_{0.3}MnO_3$ and $La_{0.7}Sr_{0.3}MnO_3$. Here, "optimal" refers to the maximum ferromagnetic Curie temperature Tc. Above T_C these materials are paramagnetic semiconductors, while below T_C they transition into ferromagnetic metals. In the vicinity of T_C, an applied magnetic field yields a dramatic decrease in the resistivity. This large negative magnetoresistance has resulted in these materials being termed colossal magnetoresistive (CMR) manganites. They are also often called half-metallic manganites referring to the complete spin polarization that occurs below T_C. Several excellent reviews of CMR materials are available.[4,5,7,9,140] Recent research has focused on the structural and electronic properties away from optimal doping, with the nature and origin of intrinsic electronic inhomogeneities receiving considerable attention.[5]

While the intense interest in manganites during the past decade[141] derives from advances in cuprate superconductivity, these materials have been investigated since their discovery in the 1950's. This initial work lead to fundamental theoretical insights related to double exchange and experimental explorations such as neutron scattering studies of their detailed magnetic structure.[142-146] In the manganites, the structural units of interest are the MnO_6 octahedra. The octahedral symmetry breaks the five-fold degeneracy of the Mn d-orbitals resulting in localized t_{2g} spins ($S = 3/2$) and higher lying e_g spins. It is in this e_g-derived band that transport occurs. Additionally, strong Hund's rule coupling leads to slaving of the e_g to the t_{2g} spins, an essential ingredient to the so-called double exchange.

In the double exchange model, electron transport between adjacent Mn ions via an intervening oxygen orbital is enhanced if the core spins on adjacent sites are parallel. However, it is now realized that the double exchange model alone cannot account for CMR behavior since the magnitude of the resistivity in the paramagnetic phase is larger than spin scattering predictions.[147,148] Coherent lattice effects such as the Jahn-Teller distortion of the MnO_6 octahedron also affect the charge transport. The simple picture is that in the paramagnetic phase lattice distortions can follow the carriers from site to site since disorder (of the t_{2g} spins) reduces the carrier kinetic energy resulting in polaronic transport. Ferromagnetic ordering increases the carrier kinetic energy. Hopping from site to site becomes too rapid for the lattice distortions to follow the carriers, resulting in a metallic state (though polaronic signatures persist below T_C). While the ultimate origin of CMR in the manganites has not been established, it is clear that the spins and polaronic behavior are basic ingredients to consider.

In the quest to more fully understand the origin of CMR, many other materials have been synthesized and characterized.[149] A particularly important class of materials in this regard are the *pyrochlores* such as $Tl_2Mn_2O_7$, which also display a pronounced negative magnetoresistance.[150,151] In $Tl_2Mn_2O_7$, the transition temperature is T_C = 120 K. Pyrochlores at first appear quite similar to perovskite manganites: both exhibit CMR, and MnO_6 octahedrons are equally important structural subunits. However, experimental and theoretical studies have highlighted important differences. In particular, in pyrochlores double exchange and Jahn-Teller effects are negligible due to the low carrier density and the absence of the Jahn-Teller Mn^{3+} ion. In addition, separate subsystems are responsible for ferromagnetic ordering (Mn 3*d* electrons, t_{2g} with $S = 3/2$ as in manganites) and conduction properties (Tl 6s electrons). The ferromagnetic ordering of the Mn^{4+} sublattice likely occurs through frustrated superexchange between Mn on adjacent sites. Below T_C, indirect exchange between the Mn and Tl orbitals causes a band of primarily Tl 6*s* character to shift below the Fermi level. It thus appears that the microscopic origin of CMR in pyrochlores and manganites is quite different, though the possibility remains that CMR in both materials derives from mesoscopic effects related to intrinsic electronic inhomogeneities. Below, we briefly discuss time-integrated infrared spectra of $La_{0.7}Ca_{0.3}MnO_3$ and $Tl_2Mn_2O_7$, followed by a description of time-resolved studies.[152-155] These THz studies provide insight into their fundamental properties and highlight important differences between these half-metallic correlated materials.

4.2 OPTICAL CONDUCTIVITY AND SPECTRAL WEIGHT TRANSFER

For the cuprates we discussed how upon entering the superconducting state spectral weight transfers from the Drude-like response to the condensate response represented as a Dirac delta function at zero frequency. In the manganites, spectral weight transfer also occurs as a function of temperature.[155] However, for these materials the spectral weight transfer occurs from higher energies (~1 eV) to a coherent Drude-like response with the crossover from paramagnetic semiconductor to ferromagnetic metal. This spectral weight transfer is intimately related to the CMR effect in DC conductivity measurements and involves the spin and lattice degrees of freedom. Figure 18 shows the temperature dependence of the optical conductivity from 0.2 to 5 eV as a function of temperature for $La_{0.7}Ca_{0.3}MnO_3$ (T_C ~ 260K).[155] This clearly shows spectral weight transfer with decreasing temperature and the development of a Drude peak centered at zero frequency. In Ref. 155, a detailed discussion of the various features of the optical conductivity has been presented. The broad feature at ~1.0 eV has been interpreted in terms of the photon-induced hopping of Jahn-Teller polarons. With decreasing temperature it is this Jahn-Teller peak that partially evolves into a metallic response below T_C. This is just as discussed above, in that with increasing spin polarization the increased carrier kinetic energy is sufficient to overcome polaronic trapping. Further details regarding the higher energy peaks can be found in Ref. 155.

In the pyrochlore $Tl_2Mn_2O_7$ (T_C = 120K), there is also a strong transfer of spectral weight from higher to lower energies with decreasing temperature.[153] However, in this material there is no high energy peak ascribable to polarons and the spectral weight transfer likely comes from higher energy (> 2eV) interband transitions consistent with the crossing of a single Tl 6*s* band as the ferromagnetic half-metallic state develops. Figure 19 shows the temperature dependence of the reflectivity for $Tl_2Mn_2O_7$. At 295 and 160 K, the carrier density is very low such that the phonons are clearly observable. At 110K, the development of a Drude peak occurs and it is fully developed at 40 K (though the phonons are still not fully screened). Comparing the 40K data with Fig. 1(b), we can see that the response is entirely consistent with Drude-like behavior including the dramatic decrease in the reflectivity at ω_s which dips and then rises back up to a value consistent with ε_∞. This behavior is quite different than in the manganites which are much more spectrally congested due to the distinct polaronic response. In $Tl_2Mn_2O_7$, the carrier density below T_C increases as the square of the magnetization to a maximum value of $n \approx 10^{19}$ cm^{-3}, about two orders of magnitude smaller than in manganites.

4.3 Dynamic spectral weight transfer in manganites

Figure 20 shows the results of THz-TDS and optical-pump THz-probe measurements on a 100-nm thick film of $La_{0.7}Ca_{0.3}MnO_3$ grown on $LaAlO_3$.[152,156] In panel (a), the real conductivity is plotted as a function of frequency at various temperatures. These conductivity measurements are in the regime $\omega\tau \ll 1$ as indicated by the flat frequency response. A large increase in the conductivity results with decreasing temperature, up to a value of $\approx 6\times10^3\ \Omega^{-1}$cm^{-1} at $T = 4$ K which is similar to poor metals. Figure 20(b) shows the temperature dependence at 0.7 THz. The solid line is a fit with $\sigma(T) = \sigma_0 \exp(M(T)/M_0)$, where $M(T) \propto (1-T/T_C)^\beta$ is the magnetization and $\beta = 0.33$. The results are in good agreement with DC resistivity measurements. The spin ordering thus clearly plays a role in determining the magnitude of the conductivity. However, as we will see from the ultrafast measurements, thermally disordered phonons (i.e. not polarons) are also quite important.

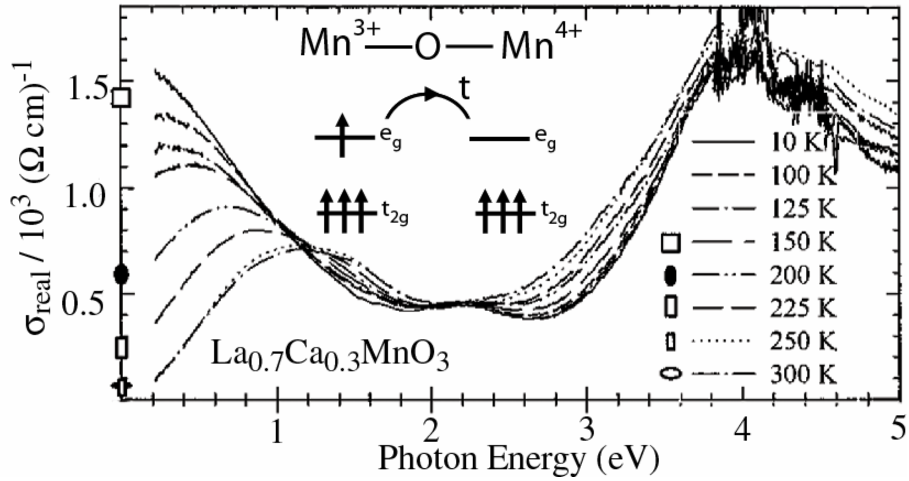

Fig. 18 Optical conductivity in $La_{0.7}Ca_{0.3}MnO_3$ as a function of photon energy at various temperatures. The inset gives a schematic depiction of double exchange. Reprinted figure with permission from Ref. 155. © 1998 by the American Physical Society.

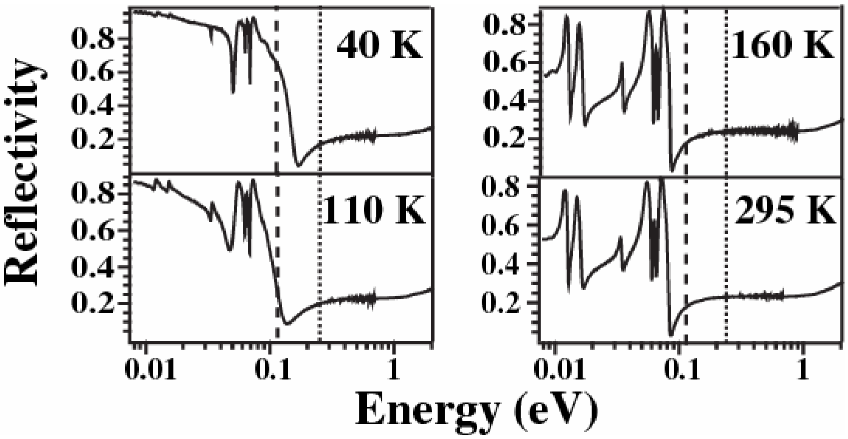

Fig. 19 Infrared reflectivity in $Tl_2Mn_2O_7$ at various temperatures.

Figure 20(c) and (d) show the dynamic changes in conductivity following photoexcitation with 100 fs 1.55 eV pulses at $T = 15$ and 180 K, respectively.[152,156] A two-component conductivity dynamics is observed following the creation of a nonthermal electron distribution. Relaxation of this hot quasiparticle distribution cools through phonon emission. This corresponds to the fast resolution-limited component in the data. The longer timescale is in turn related to the spin-lattice thermalization, where spins eventually come into thermal equilibrium with the phonons. Between 15 and 180 K, there is a strong change in the relative amplitudes of these two components: the fast electron-phonon related decrease in the conductivity and that related to spin-lattice thermalization. At low temperature, the conductivity decrease is dominated by electron-phonon relaxation, while closer to T_C

the spin-lattice thermalization component becomes more dominant. It is possible, using the time-integrated and time-dependent data in Fig. 20 (and more data at other temperatures), to extrapolate the conductivity in the T_S-T_L plane by expanding $\ln(\sigma(T_S, T_L))$ in a power series and performing a least squares fit. T_S is the spin temperature and T_L is the lattice temperature. This fitting procedure has been accomplished for $La_{0.7}Ca_{0.3}MnO_3$ to third order in T_S and T_L. The results are shown in Fig. 21 as contours of constant $\ln(\sigma)$ in the T_S-T_L plane.[152,156] Conventional measurements do not deviate from equilibrium as indicated by the white diagonal line in the figure. However, the optical-pump THz-probe experiment, while starting from a point on the equilibrium line allows for access to the portion of the T_S-T_L plane below the diagonal since the excited electrons preferentially couple to the phonons during the initial 2 ps. This optically-induced change in the phonon temperature is shown by the solid black arrow. The magnitude of this change is given by z/C_L where z is the absorbed laser energy and C_L is the lattice specific heat. The sample then returns to the equilibrium line as shown by the dashed arrows with the slope C_L/C_S (where C_S is the specific heat due to the spins). Depending on the initial temperature, z, and $C_{L,S}$, the observed conductivity decrease can depend predominantly on changes in the spin temperature, the phonon temperature, or both.

When the contours of constant conductivity are nearly perpendicular to the T_L axis, the change in conductivity is dominated by the phonons. This is the case at low temperatures as shown in the Fig. 21 (label 1). However, at higher temperatures near T_C, the lines of conductivity are now nearly parallel to the T_L axis, and thus the changes in conductivity are mostly related to changes in the spin temperature (label 2). In short, changes in conductivity at low temperatures are dominated by thermally disordered phonons, while spin fluctuations and the associated polaronic correlations dominate at higher temperatures.[152,156]

4.4 CARRIER STABILIZATION IN $TL_2MN_2O_7$ THROUGH SPATIAL INHOMOGENEITY

For the manganites, the dynamics result from energy transfer from the excited quasiparticle distribution to the lattice and spin degrees of freedom. Furthermore, the metallic-like carrier densities of approximately 10^{21} cm^{-3} means that, for moderate fluences, it is not possible to excite a large fractional change in the carrier density. The pyrochlore $Tl_2Mn_2O_7$, however, has a much lower carrier density, making it possible to photoexcite a large fractional change in the carrier density. In fact, optical pumping at 1.55 eV photoexcites electrons from O 2*p* orbitals to the Tl 6*s* derived band. Furthermore this occurs (below T_C) preferentially in the minority spin band (i.e. the carries in the Tl 6*s* band have their spins oppositely oriented to the Mn t_{2g} spins). $Tl_2Mn_2O_7$ cannot be grown as a thin film and the synthesis of single crystals is accomplished using high pressure techniques.[150] Thus, optical conductivity (Fig. 19)

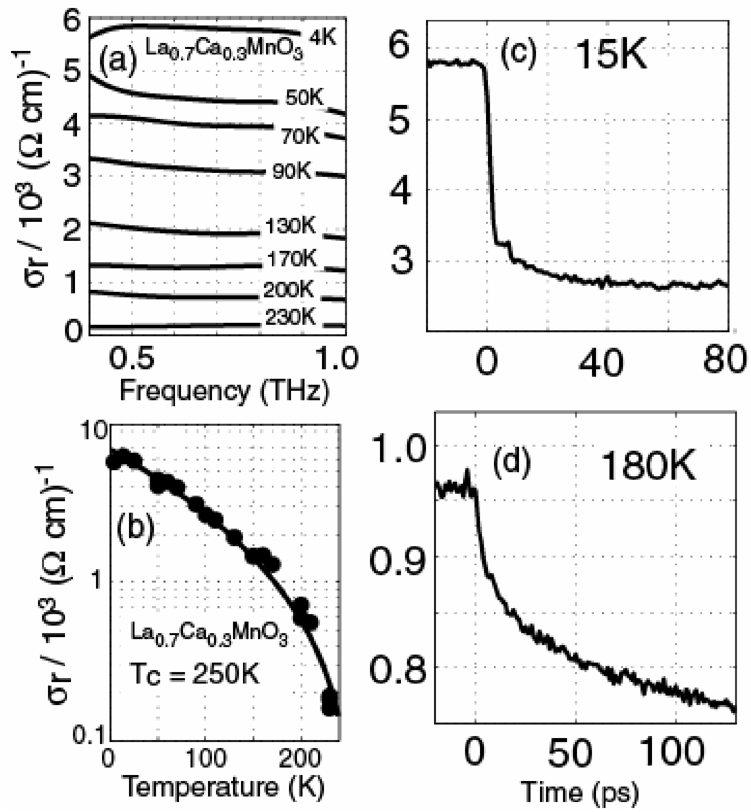

Fig. 20 (a),(b) Temperature dependent real part of conductivity in $La_{0.7}Ca_{0.3}MnO_3$ measured using THz-TDS. **(c),(d)** Two-component decrease in the conductivity following photoexcitation.

and time-resolved measurements are performed in reflection. To track the changes in the photoexcited carrier density, dynamic shifting of the plasma edge was measured at different wavelengths. In the following, results are presented for measurements at 5 μm wavelength.

Figure 22(a) shows the photoinduced changes $\Delta R/R$ in the reflectivity as a function of time at various temperatures. At all temperatures, the traces show a rapid change in reflectivity at zero delay, followed by a fast relaxation with a timescale of a few ps and a slower component with a 10-100 ps timescale. The negative $\Delta R/R$ is consistent with a photoinduced increase in the carrier density that causes a shift of the plasma edge to higher energies. The relatively fast ≈ 10 ps initial relaxation reduces the photoexcited carrier density. For $T \ll T_C$ nearly all of the carriers follow this recombination pathway. However, near and above T_C, a large offset appears in $\Delta R/R$ indicating the establishment of a long-lived carrier population.

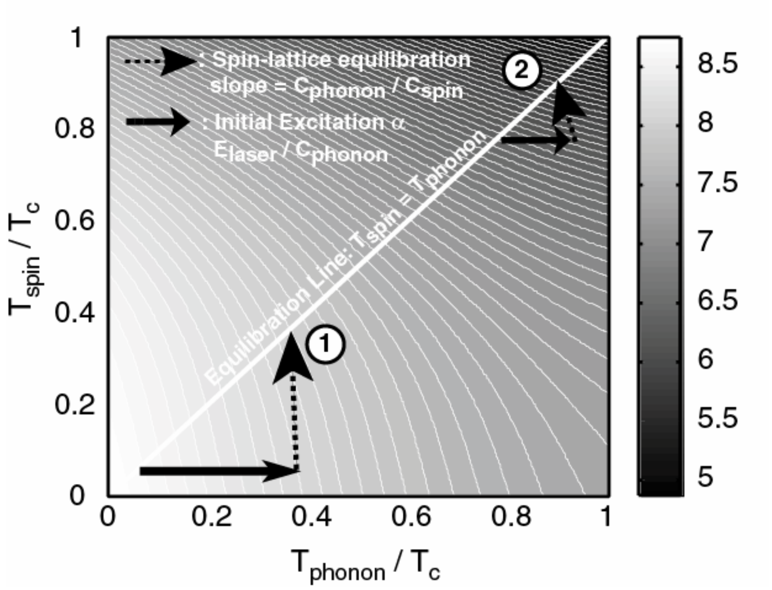

Fig. 21 Plot of the natural log of the conductivity in the phonon-spin temperature plane. The white diagonal line denotes the equilibrium line ($T_S = T_L$) of conventional time-integrated measurements. The white lines are contours of constant conductivity.

To obtain a more quantitative understanding of the charge and spin dynamics in $Tl_2Mn_2O_7$, the photoinduced change in carrier density (Δn) was extracted using the time-integrated optical conductivity and the reflectivity dynamics. The calculated photoinduced carrier density at 50 and 500 ps is plotted as a function of temperature in Fig. 22(b). In region 1 ($T < 90$ K), the photoinduced carrier density at both time delays is nearly equal, increasing as T approaches T_C. As T increases past T_C, Δn(t = 500 ps) remains nearly constant in region 2 ($90 < T < 170$ K) and then rapidly decreases in region 3 ($T > 170$ K), completely disappearing by 295 K. In the following, we focus on region 1. Further details regarding region 2 and 3 can be found in the original publication.[154]

Energy considerations and dipole selection rules dictate that the pump excitation creates *e-h* spin singlets in the minority spin manifold. At the lowest temperatures the *e-h* singlets are created in a homogeneous background of t_{2g} spins (see Fig. 23). Under these conditions, there is no energetic or dynamic constraint hindering recombination. That is, *e-h* wavefunction overlap in a spin singlet configuration occurs with a high probability, leading to recombination and a fast recovery of the carrier density (15 ps) as the data in Fig. 22(a) shows. However, with increasing temperature a long-lived carrier density develops. This indicates that a competing pathway develops that stabilizes a fraction of the photoexcited carriers against recombination.

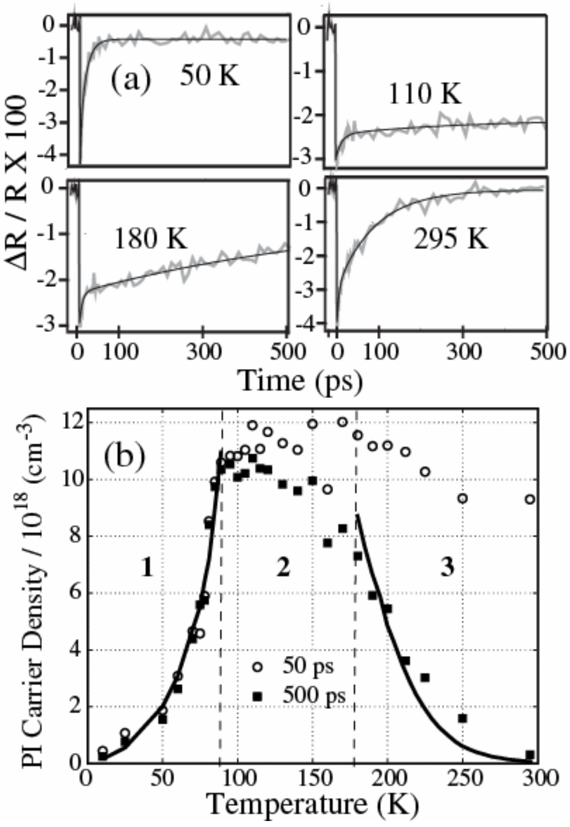

Fig. 22 **(a)** Photoinduced changes in reflectivity at 5mm for various temperatures. **(b)** Experimentally determined photoinduced carrier densities at 50 and 500 ps.

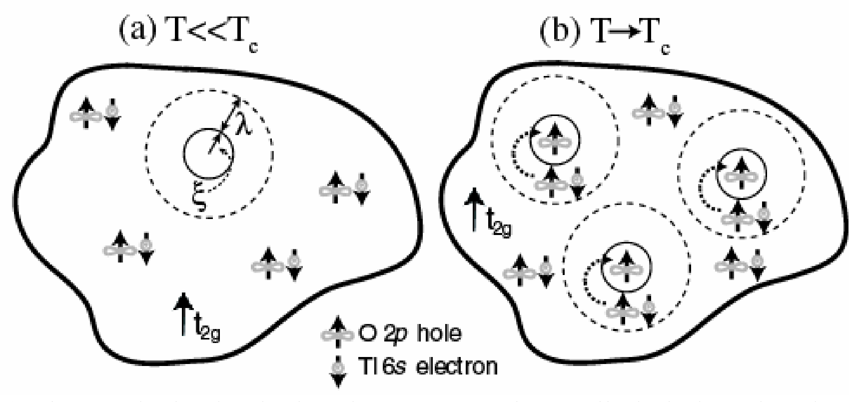

Fig. 23 **(a)** Photoexcited spin singlets for $T << T_C$. The small circle is a domain with spin down t_{2g} states and embedded in the larger area which is a domain with spin up t_{2g} states. The *e-h* pairs recombine quickly in this temperature range. **(b)** Electron-hole pairs after photoexcitation as T approaches T_C from below. In this temperature range, holes within λ of a

boundary migrate to domains of opposite t_{2g} spin orientation (dotted arrows), effectively preventing electron-hole recombination.

A route for stabilizing a fraction of the initially photoexcited carriers is through the development of spatial fluctuations (with a characteristic length scale given by the magnetic correlation length $\chi(T)$ of the Mn t_{2g} spins responsible for ferromagnetic ordering. That is, small regions of opposite t_{2g} spin develop in an otherwise homogeneous background. This is schematically depicted in Fig. 23(a) where for $T < T_C$ the density of t_{2g} (↓) domains is quite low, while it strongly increases upon approaching T_C as shown in Fig. 23(b). Of course χ is also temperature dependent, diverging at T_C as for any ferromagnet, but $\chi \approx 1$ for $T < 90$ K in region 1, yielding a correlation length of order 0.1 nm.[157] In this simple picture, we emphasize that it is therefore the density of "defects" of opposite t_{2g} orientation that capture the essential physics of carrier stabilization.

The spatial inhomogeneity that develops has important implications for photoexcited *e-h* pairs. From the bandstructure (not shown – see Ref. 154), it is energetically favorable for O 2p holes to cross a t_{2g} (↑) - t_{2g}(↓) boundary, whereas there is an energetic barrier for the Tl 6s electrons. Thus, the spatial inhomogeneity in the t_{2g} spin manifold leads to spatial segregation of the photoexcited Tl 6s electrons and O 2p holes, which in turn inhibits recombination. However, this process competes with recombination, and spatial segregation can only occur for holes that are initially created within a distance λ of a boundary as depicted in Fig. 23. The net result is that with increasing temperature the number of "defects" increases, leading to an increase in the Tl 6s carrier density since more O 2p holes are trapped.

Thus, in region 1 the amplitude of the fast relaxation component is due to recombination while that of the slow component is due to carrier stabilization. Therefore, the photoinduced carrier density at $t = 500$ ps should be proportional to the ratio of slow to fast amplitudes in the $\Delta R/R$ traces. This in turn scales with the ratio of the volume occupied by t_{2g}(↑) spins to that occupied by t_{2g}(↓) spins, including a factor $\gamma=(\lambda+\chi)^3$. Here, γ is the effective volume where the probability of trapping an O 2p hole is greater than a recombination event. This results in an expression for the excess Tl 6s electron density Δn given by

$$\Delta n = C_0 \frac{\gamma(1-M)}{2\xi^3 - \gamma(1-M)} \tag{12}$$

where the magnetization M is normalized to its saturation value and C_0 is a proportionality constant. The solid line in Fig. 22(b) shows Δn plotted as a function of temperature for $T < 90$ K, revealing good agreement with the data. This analysis yields $\lambda \sim 0.79$ unit cells, indicating that the photoexcited holes can only travel a very short distance before recombining. In summary, spatial inhomogeneity that develops in the t_{2g} spins (responsible for a decrease in M) stabilizes a fraction of the photoexcited carriers.[154]

These results are consistent with CMR in $Tl_2Mn_2O_7$ arising from carrier localization due to strong spin fluctuations without invoking phonons, which is in dramatic contrast to the results for the manganites where phonons (be they thermally disordered or of a polaronic nature) were crucial. These results also suggest that $Tl_2Mn_2O_7$ may be a particularly simple example where the transport properties are determined by intrinsic nanoscale inhomogeneity occurring near a second order phase transition.

5. SUMMARY AND OUTLOOK

We hope this chapter has revealed the potential of time-resolved THz techniques in the study of many-body correlations in bulk and nanostructured semiconductors, superconductors, and strongly-correlated transition-metal oxides. In semiconductors, we have reviewed experiments that study the free-carrier response and buildup of Coulomb correlations, distinct signatures of intra-excitonic transitions that test the analogy between *e*-*h* gases and atomic systems, and the ultrafast polarization kinetics of intersubband transitions. Time-domain THz spectroscopy provides for a direct determination of the real and imaginary parts of conductivity, which in superconductors directly reveals the quasiparticle and superfluid densities, and the excitation gap 2Δ of the correlated charge pairs. Time-resolving the conductivity dynamics, in turn, gives the most direct insight into the temporal breakup and recombination kinetics of quasiparticles in both conventional and high-T_C superconductors. Time-resolved THz spectroscopy of manganites and pyrochlores gives important insight into dynamic spectral weight transfer, quasiparticle interactions with lattice and spin degrees of freedom, and stabilization processes of carriers through spatial inhomogeneities.

Of course, these results barely scratch the surface of what is possible and within the context of dynamic studies on nanoscale and correlated materials there is still a great deal to be investigated. Intra-excitonic spectroscopy represents a rising field to investigate low-temperature carrier phases in semiconductors, where THz probes of optically-dark states are of increasing interest in the search for excitonic Bose-Einstein condensates.[38,158] There are also a number of differences in the dynamics of YBCO and Bi-2212 presented in Section 3. It is not yet clear if these differences are intrinsic to the properties of these materials or are related to experimental parameters such as the incident fluence. It would be interesting to probe the dynamics for a larger range of materials and over a broader doping range. This holds for the manganites as well where, to date, dynamic optical-pump THz-probe experiments have only been performed on optimally doped samples (e.g. those that display half-metallicity). However, as function of doping, the manganites display an enormous number of states including charge ordering, orbital ordering, and various magnetically ordered states. It will be important to understand the dynamics in each of these distinct phases especially as research on these materials focuses more and more on phenomena associated with phase coexistence.[5,140] For example, recent mid-infrared studies on $Nd_{0.5}Sr_{0.5}MnO_3$ which transitions from paramagnetic semiconductor to ferromagnetic metal to charge-ordered insulator with decreasing temperature suggest that the dynamic polaron response provides a way to probe phase coexistence.[159]

There are also a host of other materials where probing the mid or far infrared dynamics can be expected to provide considerable insight. For example, several visible and X-ray experiments have studied the dynamics of VO_2, giving insight into the insulator-metal transition and the cause-effect relationships between lattice and electronic degrees of freedom.[160,161] Recent THz experiments complement these previous studies.[162] This leads, more generally, to the idea photoinduced phase transitions both in materials where the phase transition is thermally accessible (as in VO_2) and those where photoexcitation leads to a metastable state which is not thermodynamically accessible as observed, for instance, in Ref. 163. Other examples include *f*-electron intermetallics, where hybridization between localized *f* moments and the conductions electrons results in a THz hybridization gap.[164] All-optical pump-probe studies have been utilized to probe the quasiparticle dynamics as a function of temperature and show a strong dependence on the opening of a hybridization gap[165] but, to date, there have been no experiments which directly probe the dynamics at the gap edge as reported for superconductors.[136] Finally, we mention the area of multiferroics which is becoming an increasingly active research area. In multiferroics such as $LuMnO_3$ or $Ba_{0.5}Sr_{1.5}Zn_2Fe_{12}O_{22}$, there are two coexisting order parameters with the most common being ferroelectricity and antiferromagnetism. This leads to magnetoelectric coupling where the magnetic order can be modified with an electric field or vice versa.[166-171] There is a great deal to be learned about these materials using both time-integrated and time-resolved optical spectroscopy. For example, using THz spectroscopy, electromagnons have recently been reported.[172] This suggests that optical-pump THz-probe experiments may provide insight into the dynamics and microscopic origin of magnetoelectric coupling in these materials.

In addition to probing the dynamics of other correlated-electron materials, experimental and theoretical advances are also expected to provide new opportunities. One area that seems to be very exciting is to use THz pulses with high peak electric fields as described in Section 2. Fields on the order of 1 MV/cm will enable coherent control of low-energy transitions in excitons and various nanoscale materials, and may lead to interesting nonlinear dynamics in correlated-electron materials such as superconductors, manganites, and multiferroics. The majority of optical-pump THz-probe studies to date have utilized near-IR or visible pulses for photoexcitation. It would be of enormous value to have greater spectral agility for the photoexcitation. This is challenging in the case of optical-pump THz-probe spectroscopy since the pump spot size needs to be quite large (typically several mm) for uniform excitation of the THz probe beam, while the THz probe ideally must remain sensitive requiring fairly high repetition rates. Finally, we mention the need for a more concerted theoretical effort in this area. It is true that for semiconductors sophisticated theories have been developed to investigate fundamental quantum kinetics.[173] It would be of considerable interest if this were extended to other correlated-electron materials. In this way, time-resolved THz techniques promise to provide unprecedented insight and control over the basic properties of complex materials.

Acknowledgements. We thank our many collaborators on infrared and THz spectroscopy studies reviewed here, in particular D. S. Chemla, T. Elsaesser, M. Woerner, M. A. Carnahan, A. J. Taylor, S. A. Trugman, J. Demsar, R. P. Prasankumar and many more. Preparation of this review was in part supported by the Office of Science of the U.S. Department of Energy under Contract DE-AC02-05CH11231 and by the Los Alamos National Laboratory LDRD program. We would also like to thank the authors of various papers for the permission to reproduce their figures in the preceding text.

REFERENCES

1. Basov, D. N. and Timusk, T., Electrodynamics of high-T_C superconductors, *Rev. Mod. Phys.* 77, 721-779, 2005.
2. Bednorz, J. G. and Müller, K. A., Possible high T_C superconductivity in the Ba-La-Cu-O system, *Z. Phys. B* 64, 189-93, 1986.
3. Bonn, D. A., Are high-temperature superconductors exotic?, *Nature Physics* 2, 159-168, 2006.
4. Coey, J. M. D., Viret, M., and von Molnar, S., Mixed-valence Manganites, *Adv. Phys.* 48, 167-293, 1999.
5. Dagotto, E., Hotta, T., and Moreo, A., Colossal magnetoresistant materials: the key role of phase separation, *Phys. Rep.* 344, 1-153, 2001.
6. Fazekas, P., *Lecture Notes on Electron Correlation and Magnetism* World Scientific, Singapore, 1999.
7. Imada, M., Fujimori, A., and Tokura, Y., Metal-insulator transitions, *Rev. Mod. Phys.* 70, 1039-1263, 1998.
8. Orenstein, J. and Millis, A. J., Advances in the physics of high-temperature superconductivity, *Science* 288, 468-474, 2000.
9. Salamon, M. B. and Jaime, M., The physics of manganites: Structure and transport., *Rev. Mod. Phys.* 73, 583-628, 2001.
10. Tinkham, M., *Introduction to Superconductivity*, 2nd ed. McGraw-Hill, New York, 1996.

11. Chemla, D. S., Correlation and coherence in semiconductors, *Comptes Rendus De L Academie Des Sciences Serie Iv Physique Astrophysique* 2 (10), 1427-1438, 2001.

12. Shah, J., *Ultrafast Spectroscopy of Semiconductors and Semiconductor Nanostructures* Springer Verlag, Berlin, 1999.

13. Nuss, M. C. and Orenstein, J., in *Millimeter and Submillimeter Wave Spectroscopy of Solids*, Grüner, G. Springer Verlag, Berlin, 1998.

14. Cooper, S. L., Optical Spectroscopic Studies of Metal Insulator Transistions in Perovskite-Related Oxides, *Structure and Bonding* 98, 161-218, 2001.

15. Li, X. Q., Zhang, T. H., Borca, C. N., and Cundiff, S. T., Many-body interactions in semiconductors probed by optical two-dimensional Fourier transform spectroscopy, *Phys. Rev. Lett.* 96, 057406, 2006.

16. Hickey, B. J., Morgan, G. J., and Howson, M. A., Basic Electron Transport, in *Spin Electronics*, Thornton, M. J. andZiese, M. Springer-Verlag, 2001.

17. Puchkov, A. V., Basov, D. N., and Timusk, T., The pseugap state in high-T_C superconductors: an infrared study, *J. Phys. Cond. Mat.* 8, 1996.

18. Tsai, T.-R., Chen, S.-J., Chang, C.-F., Hsu, S.-H., and Lin, T.-Y., Terahertz response of GaN thin films, *Optics Express* 14 (11), 4898-4907, 2005.

19. Jeon, T.-I. and Grischkowsky, D., Nature of Conduction in Doped Silicon, *Phys. Rev. Lett.* 78, 1106-1109, 1997.

20. Lui, K. P. H. and Hegmann, F. A., Ultrafast carrier relaxation in radiation-damaged silicon on sapphire studied by optical-pump-terahertz-probe experiments, *Appl. Phys. Lett.* 78, 3478-3480, 2001.

21. Prasankumar, R. P., Scopatz, A., Hilton, D. J., Taylor, A. J., Averitt, R. D., Zide, J. M., and Gossard, A. C., Carrier dynamics in self-assembled ErAs nanoislands embedded in GaAs measured by optical-pump terahertz-probe spectroscopy, *Appl. Phys. Lett.* 86, 201107, 2005.

22. Schmuttenmaer, C. A., Exploring dynamics in the far-infrared with terahertz spectroscopy, *Chemical reviews* 104, 1759-1779, 2004.

23. Huber, R., Tauser, F., Brodschlem, A., Bichler, M., Abstreiter, G., and Leitenstorfer, A., How many-particle interactions developafter ultrafast excitation of an electron-hole plasma, *Nature* 414, 286-289, 2001.

24. Wu, Q. and Zhang, X.-C., Free-space electro-optics sampling of mid-infrared pulses, *Applied Physics Letters* 71, 1285 - 1286, 1997.

25. Kaindl, R. A., Smith, D. C., Joschko, M., Hasselbeck, M. P., Woerner, M., and Elsaesser, T., Femtosecond infrared pulses tunable from 9 to 18 mu m at an 88-MHz repetition rate, *Opt. Lett.* 23, 861-863, 1998.

26. Bartel, T., Gaal, P., Reimann, K., Woerner, M., and Elsaesser, T., Generation of single-cycle THz transients with high electric-field amplitudes, *Opt. Lett.* 30, 2805-2807, 2005.

27. You, D., Jones, R. R., Bucksbaum, P. H., and Dykaar, D. R., Generation of high-power sub-single-cycle 500-fs electromangetic pulses, *Opt. Lett.* 18, 290-292, 1993.

28. Feurer, T., Vaughan, J. C., and Nelson, K. A., Spatiotemporal coherent control of lattice vibrational waves, *Science* 299, 374-377, 2003.

29. van Tilborg, J., Schroeder, C. B., Filip, C. V., Toth, C., Geddes, C. G. R., Fubiani, G., Huber, R., Kaindl, R. A., Esarey, E., and Leemans, W. P., Temporal

characterization of femtosecond laser-plasma-accelerated electron bunches using terahertz radiation, *Phys. Rev. Lett.* 96, 014801, 2006.

[30] Gaal, P., Reimann, K., Woerner, M., Elsaesser, T., Hey, R., and Ploog, K. H., Nonlinear Terahertz Reponse of n-Type GaAs, *Phys. Rev. Lett.* 96, 187402, 2006.

[31] Chemla, D. S. and Shah, J., Many-body and correlation effects in semiconductors, *Nature* 411, 549-557, 2001.

[32] Haken, H., *Fortschr. Phys.* 38 (271), 1958.

[33] Nikitine, S., *J. Phys. Chem. Solids* 45, 949, 1984.

[34] Timusk, T., Far-infrared absorption study of exciton ionization in germanium, *Phys. Rev. B* 13, 3511-3514, 1976.

[35] Cerne, J., Kono, J., Sherwin, M. S., Sundaram, M., Gossard, A. C., and Bauer, G. E. W., Terahertz Dynamics of Excitons in GaAs/AlGaAs Quantum Wells, *Phys. Rev. Lett.* 77, 1131-1134, 1996.

[36] Groeneveld, R. H. M. and Grischkowsky, D., Picosecond time-resolved far-infrared experiments on carriers and excitons in GaAs-AlGaAs multiple quantum wells, *J. Opt. Soc. Am. B* 11, 2502, 1994.

[37] Kaindl, R. A., Carnahan, M. A., Hagele, D., Lovenich, R., and Chemla, D. S., Ultrafast terahertz probes of transient conducting and insulating phases in an electron-hole gas, *Nature* 423, 734 - 738, 2003.

[38] Kubouchi, M., Yoshioka, K., Shimano, R., Mysyrowicz, A., and Kuwata-Gonokami, M., Study of Orthoexciton-to-Paraexciton Conversion in Cu_2O by Excitonic Lyman Spectroscopy, *Phys. Rev. Lett.* 94, 016403, 2005.

[39] Johnsen, K. and Kavoulakis, G. M., Probing Bose-Einstein Condensation of Excitons with Electromagnetic Radiation, *Phys. Rev. Lett.* 86, 858 - 861, 2001.

[40] Kira, M., Hoyer, W., Stroucken, T., and Koch, S. W., Exciton Formation in Semiconductors and the Influence of a Photonic Environment, *Phys. Rev. Lett.* 87, 176401, 2001.

[41] Koch, S. W., Kira, M., Khitrova, G., and Gibbs, H. M., Semiconductor excitons in new light, *Nature Materials* 5, 523 - 531, 2006.

[42] Ekenberg, U. and Altarelli, M., Exciton binding energy in a quantum well with inclusion of valence-band coupling and nonparabolicity, *Phys. Rev. B* 35, 7585, 1987.

[43] Haug, H. and Koch, S. W., *Quantum theory of the Optical and Electronic Properties of Semiconductors* World Scientific, Signapore, 2004.

[44] Kaindl, R. A., Hägele, D., Carnahan, M. A., and Chemla, D. S., Transient terahertz spectroscopy of excitons and unbound carriers in quasi two-dimensional electron-hole gases, (unpublished), 2006.

[45] Oh, I. K., Singh, J., Thilagam, A., and Vengurlekar, A. S., Exciton formation assisted by LO phonons in quantum wells, *Phys. Rev. B* 62, 2045-2050, 2000.

[46] Selbmann, P. E., Gulia, M., Rossi, F., Molinari, E., and Lugli, P., Coupled free-carrier and exciton relaxation in optically excited semiconductors, *Phys. Rev. B* 54, 4660, 1996.

[47] Siantidis, K., Axt, V. M., and Kuhn, T., Dynamics of exciton formation for near band gap excitations, *Phys. Rev. B* 65, 035303, 2002.

[48] Huber, R., Kaindl, R. A., Schmid, B. A., and Chemla, D. S., Broadband terahertz study of excitonic resonances in the high-density regime in $GaAs/Al_xGa_{1-x}As$ quantum wells, *Phys. Rev. B* 72, 161314, 2005.

[49] Huber, R., Schmid, B. A., Shen, Y. R., Chemla, D. S., and Kaindl, R. A., Stimulated Terahertz Emission from Intra-Excitonic Transitions in Cu_2O, *Phys. Rev. Lett.* 96, 017402, 2006.

[50] Kira, M. and Koch, S. W., Exciton-Population Inversion and Terahertz Gain in Semiconductors Excited to Resonance, *Phys. Rev. Lett.* 93, 076402, 2004.

[51] Uihlein, C., Fröhlich, D., and Kenklies, R., Investigation of exciton fine structure in Cu_2O, *Phys. Rev. B* 23, 2731, 1981.

[52] Keldysh, L. V. and Kozlov, A. N., *Sov. Phys. JETP* 27, 521, 1968.

[53] Butov, L. V., Gossard, A. C., and Chemla, D. S., Macroscopically ordered state in an exciton system, *Nature* 418, 751-754, 2002.

[54] Lai, C. W., Zoch, J., Gossard, A. C., and Chemla, D. S., Phase diagram of degenerate exciton systems, *Science* 303, 503 - 506, 2004.

[55] Snoke, D., Spontaneous Bose Coherence of Excitons and Polaritons, *Science* 298, 1368, 2002.

[56] O'Hara, K. E. and Wolfe, J. P., Relaxation kinetics of excitons in cuprous oxide, *Phys. Rev. B* 62, 12909-12922, 2000.

[57] Jang, J. I. and Wolfe, J. P., Biexcitons in the semiconductor Cu_2O: An explanation of the rapid decay of excitons, *Phys. Rev. B* 72, 241201, 2005.

[58] Jang, J. I. and Wolfe, J. P., Relaxation of stress-split orthoexcitons in Cu_2O, *Phys. Rev. B* 73, 075207, 2006.

[59] Jolk, A., Jörger, M., and Klingshirn, C., Exciton lifetime, Auger recombination, and exciton transport by calibrated difference absorption spectroscopy in Cu_2O, *Phys. Rev. B* 65, 245209, 2002.

[60] Göppert, M., Becker, R., Maier, C., Jörger, M., Jolk, A., and Klingshirn, C., Infrared Absorption by Excitons in Cuprous Oxide, *Int. J. of Mod. Phys. B* 15, 3615 - 3618, 2001.

[61] Jörger, M., Tsitsishvili, E., Fleck, T., and Klingshirn, C., Infrared absorption by excitons in Cu2O, *phys. stat. sol. (b)* 238, 470-473, 2003.

[62] Karpinska, K., Mostovoy, M., van der Vegte, M. A., Revcolevschi, A., and van Loosdrecht, P. H. M., Decay and coherence of two-photon excited yellow orthoexcitons in Cu_2O, *Phys. Rev. B* 72, 155201, 2005.

[63] Kuwata-Gonokami, M., Observation of ortho and para-excitons by time-resolved excitonic Lyman spectroscopy, *Solid State Comm.* 134, 127 - 133, 2005.

[64] Kuwata-Gonokami, M., Kubouchi, M., Shimano, R., and Mysyrowicz, A., Time-resolved Excitonic Lyman Spectroscopy of Cu_2O, *J. Phys. Soc. Jpn.* 73, 1065 - 1069, 2004.

[65] Kamgar, A., Kneschaurek, P., Dorda, G., and Koch, J. F., Resonance Spectroscopy of Electronic Levels in a Surface Acumulation Layer, *Phys. Rev. Lett.* 32, 1251 - 1254, 1974.

[66] West, L. C. and Eglash, S. J., First observation of an extremely large-dipole infrared transition within the conduction band of a GaAs quantum well, *Appl. Phys. Lett.* 46, 1156 - 1158, 1985.

[67] Faist, J., Capasso, F., Sivco, D. L., Sirtori, C., Hutchinson, A. L., and Cho, A. Y., Quantum Cascade Laser, *Science* 264, 553 - 556, 1994.

[68] Kohler, R., Tredicucci, A., Beltram, F., Beere, H. E., Linfield, E. H., Davies, A. G., Ritchie, D. A., Iotti, R. C., and Rossi, F., Terahertz semiconductor-heterostructure laser, *Nature* 417, 156 - 159, 2002.

[69] Seilmeier, A., Hübner, H.-J., Abstreiter, G., Weimann, G., and Schlapp, W., Intersubband relaxation in GaAs-$Al_xGa_{1-x}As$ quantum well structures observed directly by an infrared bleaching technique, *Phys. Rev. Lett.* 59, 1345 - 1348, 1987.

[70] Bauerle, R. J., Elsaesser, T., Lobentanzer, H., Stolz, W., and Ploog, K., Transient reshaping of intersubband absorption spectra due to hot-electrons in a modulation-doped multipe-quantum-well structure, *Phys. Rev. B* 40, 10002-10005, 1989.

[71] Lutgen, S., Kaindl, R. A., Woerner, M., Elsaesser, T., Hase, A., and Kunzel, H., Nonlinear intersubband absorption of a hot quasi-two-dimensional electron plasma studied by femtosecond infrared spectroscopy, *Phys. Rev. B* 54, 17343-17346, 1996.

[72] Lutgen, S., Kaindl, R. A., Woerner, M., Elsaesser, T., Hase, A., Kunzel, H., Gulia, M., Meglio, D., and Lugli, P., Nonequilibrium dynamics in a quasi-two-dimensional electron plasma after ultrafast intersubband excitation, *Phys. Rev. Lett.* 77, 3657-3660, 1996.

[73] Kaindl, R. A., Wurm, M., Reimann, K., Woerner, M., Elsaesser, T., Miesner, C., Brunner, K., and Abstreiter, G., Ultrafast dynamics of intersubband excitations in a quasi-two-dimensional hole gas, *Phys. Rev. Lett.* 86, 1122-1125, 2001.

[74] Heyman, J. N., Unterrainer, K., Craig, K., Williams, J., Sherwin, M. S., Campman, K., Hopkins, P. F., Gossard, A. C., Murdin, B. N., and Langerak, C. J. G. M., Far-Infrared Pump-Probe Measurements of the Intersubband Lifetime in an AlGaAs/GaAs Coupled-Quantum Well, *Appl. Phys. Lett.* 68, 3019 - 3021, 1996.

[75] Müller, T., Parz, W., Strasser, G., and Unterrainer, K., Influence of carrier-carrier interaction on time-dependent intersubband absorption in a semiconductor quantum well, *Phys. Rev. B* 70, 155324, 2004.

[76] Bonvalet, A., Nagle, J., Berger, V., Migus, A., Martin, J.-L., and Joffre, M., Femtosecond Infrared Emission Resulting from Coherent Charge Oscillations in Quantum Wells, *Phys. Rev. Lett.* 76, 4392 - 4395, 1996.

[77] Planken, P. C. M., Nuss, M. C., Brener, I., Goossen, K. W., Luo, M. S. C., Chuang, S.-L., and Pfeiffer, L., Terahertz emission in single quantum wells after coherent optical excitation of light hole and heavy hole excitons, *Phys. Rev. Lett.* 69, 3800 - 3803, 1992.

[78] Roskos, H. G., Nuss, M. C., Shah, J., Leo, K., Miller, D. A. B., Fox, A. M., Schmitt-Rink, S., and Köhler, K., Coherent submillimeter-wave emission from charge oscillations in a double-well potential, *Phys. Rev. Lett.* 68, 2216 - 2219, 1992.

[79] Bratschitsch, R., Muller, T., Kersting, R., Strasser, G., and Unterrainer, K., Coherent terahertz emission from optically pumped intersubband plasmons in parabolic quantum wells, *Appl. Phys. Lett.* 76, 3501 - 3503, 2000.

[80] Waschke, C., Roskos, H. G., Schwedler, R., Leo, K., Kurz, H., and Köhler, K., Coherent submillimeter-wave emission from Bloch oscillations in a semiconductor superlattice, *Phys. Rev. Lett.* 70, 3319 - 3322, 1993.

[81] Kaindl, R. A., Lutgen, S., Woerner, M., Elsaesser, T., Nottelmann, B., Axt, V. M., Kuhn, T., Hase, A., and Künzel, H., Ultrafast dephasing of coherent intersubband polarizations in a quasi-two-dimensional electron plasma, *Phys. Rev. Lett.* 80, 3575-3578, 1998.

[82] Kaindl, R. A., Reimann, K., Woerner, M., Elsaesser, T., Hey, R., and Ploog, K. H., Homogeneous broadening and excitation-induced dephasing of intersubband transitions in a quasi-two-dimensional electron gas, *Phys. Rev. B* 63, 161308, 2001.

[83] Eickemeyer, F., Reimann, K., Woerner, M., Elsaesser, T., Barbieri, S., Sirtori, C., Strasser, G., Muller, T., Bratschitsch, R., and Unterrainer, k., Ultrafast coherent electron transport in semiconductor quantum cascade structures, *Phys. Rev. Lett.* 89, 047402, 2002.

[84] Carter, S. G., Ciulin, V., Hanson, M., Huntington, A. S., Wang, S., Gossard, A. C., Coldren, L. A., and Sherwin, M. S., Terahertz-optical Mixing in Undoped and Doped GaAs Quantum Wells From Excitonic to Electronic Intersubband Transitions, *Phys. Rev. B* 72, 155309, 2005.

[85] Craig, K., Galdrikian, B., Heyman, J. N., Markelz, A. G., Williams, J. B., Sherwin, M. S., Campman, K., Hopkins, P. F., and Gossard, A. C., Undressing a Collective Intersubband Excitation in a Quantum Well, *Phys. Rev. Lett.* 76, 2382 - 2385, 1996.

[86] Luo, C. W., Reimann, K., Woerner, M., Elsaesser, T., Hey, R., and Ploog, K. H., Phase-Resolved Nonlinear Response of a Two-Dimensional Electron Gas under Femtosecond Intersubband Excitation, *Phys. Rev. Lett.* 92, 047402, 2004.

[87] Shih, T., Reimann, K., Woerner, M., Elsaesser, T., Waldmuller, I., Knorr, A., Hey, R., and Ploog, K., Nonlinear response of radiatively coupled intersubband transitions of quasi-two-dimensional electrons, *Phys. Rev. B* 72, 195338, 2005.

[88] Waldmueller, I., Chow, W. W., and Knorr, A., Influence of radiative coupling on coherent Rabi intersubband oscillations in multiple quantum wells, *Phys. Rev. B* 73, 035433, 2006.

[89] Cole, B. E., Williams, J. B., King, B. T., Sherwin, M. S., and Stanley, C. R., Coherent manipulation of semiconductor quantum bits with terahertz radiation, *Nature* 410, 60 - 63, 2001.

[90] Frogley, M. D., Dynes, J. F., Beck, M., Faist, J., and Phillips, C. C., Gain without inversion in semiconductor nanostructures, *Nature Materials* 5, 175 - 178, 2006.

[91] Sherwin, M. S., Imamoglu, A., and Montroy, T., Quantum computation with quantum dots and terahertz cavity quantum electrodynamics, *Phys. Rev. A* 60, 3508 - 3514, 1999.

[92] Batista, A. A., Pulse-driven interwell carrier transfer in n-type doped asymmetric double quantum wells, *Phys. Rev. B* 73, 075305, 2006.

[93] Paspalakis, E., Tsaousidou, M., and Terzis, A. F., Coherent manipulation of a strongly driven semiconductor quantum well, *Phys. Rev. B* 73, 125344, 2006.

[94] Bardeen, J., Cooper, L. N., and Schrieffer, J. R., Theory of superconductivity, *Phys. Rev.* 108, 1175-1204, 1957.

[95] Mattis, D. C. and Bardeen, J., Theory of the Anomalous Skin Effect in Normal and Superconducting Metals, *Phys. Rev.* 111, 412 - 417, 1958.

[96] Glover, R. E. and Tinkham, M., Conductivity of Superconducting Films for Photon Energies between 0.3 and 40kTc, *Phys. Rev.* 108, 243-256, 1957.

[97] Miller, B. I. and Dayem, A. H., Relaxation and recombination times of quasiparticles in superconducting Al thin films, *Phys. Rev. Lett.* 18 (23), 1000-1004, 1967.

[98] Rothwarf, A. and Taylor, B. N., Measurement of recombination lifetimes in superconductors, *Phys. Rev. Lett.* 3, 27-30, 1967.

[99.] Gray, K. E., *Nonequilibrium Superconductivity, Phonons, and Kaptiza Boundaries* Plenum, New York, 1981.

[100.] Kaplan, S. B., Chi, C. C., Langenberg, D. N., Chang, J. J., Jafarey, S., and Scalapino, D. J., Quasiparticle and phonon lifetimes in superconductors, *Phys. Rev. B* 14, 4854-4873, 1976.

[101.] Schuller, I. and Gray, K. E., Experimental observation of the relaxation time of the order parameter in superconductors, *Phys. Rev. Lett.* 36, 429-432, 1976.

[102.] Testardi, L. R., Destruction of superconductivity by laser light, *Phys. Rev. B* 4, 2189-2196, 1971.

[103.] Allen, J. W., Aronson, M., Boebinger, G. S., Broholm, C. L., Cooper, S. L., Crow, J. E., Hammel, P. C., and Lander, G., Future probes in materials science, *Physica B* 318, 12-23, 2002.

[104.] Eesley, G. L., Observation of non-equilibrium heating in copper, *Phys. Rev. Lett.* 51, 2140-2143, 1983.

[105.] Schoenlein, R. W., Lin, W. Z., Fujimoto, J. G., and Eesley, G. L., Femtosecond studies of nonequilibrium electronic processes in metals, *Phys. Rev. Lett.* 58, 1680-1683, 1987.

[106.] Brorson, S. D., Buhleier, R., Trofimov, I. E., White, J. O., Ludwig, C., Balakirev, F. F., Habermeier, H.-U., and Kuhl, J., Electrodynamics of high-temperature superconductors investigated with coherent terahertz pulse spectroscopy, *J. Opt. Soc. Am. B* 13, 1979-1993, 1996.

[107.] Demsar, J., Podobnik, B., Kabanov, V. V., Wolf, T., and Mihailovic, D., Superconducting gap Delta(c), the pseudogap Delta(p), and pair fluctuations above T-c in overdoped Y1-xCaxBa2Cu3O7-delta from femtosecond time-domain spectroscopy, *Phys. Rev. Lett.* 82, 4918-4921, 1999.

[108.] Han, S. G., Vardeny, Z. V., Wong, K. S., Symko, O. G., and Koren, G., Femtosecond optical detection of quasiparticle dynamics in high-T_C $YBa_2Cu_3O_{7-\delta}$ superconducting thin films, *Phys. Rev. Lett.* 65, 2708, 1990.

[109.] Nuss, M. C., Goossen, K. W., Mankiewich, P. M., and O'Malley, M. L., Terahertz surface impedance of thin $YBa_2Cu_3O_7$ superconducting films, *Appl. Phys. Lett.* 58, 2561 - 2563, 1991.

[110.] Palmer, L. H. and Tinkham, M., Far-Infrared Absorption in Thin Superconducting Lead Films, *Phys. Rev.* 165, 588–595, 1968.

[111.] Jaekel, C., Waschke, C., Roskos, H. G., Kurz, H., Prusseit, W., and Kinder, W., Surface resistance and penetration depth of $YBa_2Cu_3O_{7-\delta}$ thin films on silicon at ultrahigh frequencies, *Appl. Phys. Lett.* 64, 3326 - 3328, 1994.

[112.] Nuss, M. C., Mankiewich, P. M., O'Malley, M. L., Westerwick, E. H., and Littlewood, P. B., Dynamic conductivity and coherence peak in $YBa_2Cu_3O_7$ superconductors, *Phys. Rev. Lett.* 66, 3305–3308, 1991.

[113.] Wilke, I., Khazan, M., Rieck, C. T., Kuzel, P., Kaiser, T., Jaekel, C., and Kurz, H., Terahertz surface resistance of high temperature superconducting thin films, *J. Appl. Phys.* 87, 2984 - 2988, 2000.

[114.] Kaindl, R. A., Carnahan, M. A., Orenstein, J., Chemla, D. S., Christen, H. M., Zhai, H. Y., Paranthaman, M., and Lowndes, D. H., Far-infrared optical conductivity gap in superconducting MgB_2 films, *Phys. Rev. Lett.* 88, 027003, 2002.

[115] Nagamatsu, J., Nakagawa, N., Muranaka, T., Zenitani, Y., and Akimitsu, J., Superconductivity at 39 K in magnesium diboride, *Nature* 410, 63 - 64, 2001.

[116] Born, M. and Wolf, E., *Principles of Optics* University Press, Cambridge, 1999.

[117] Choi, H. J., Roundy, D., Sun, H., Cohen, M. L., and Louie, S. G., The origin of the anomalous superconducting properties of MgB_2, *Nature* 418, 758 - 760, 2002.

[118] Kortus, J., Mazin, I. I., Belashchenko, K. D., Antropov, V. P., and Boyer, L. L., Superconductivity of Metallic Boron in MgB_2, *Phys. Rev. Lett.* 86, 4656 - 4659, 2001.

[119] Liu, A. Y., Mazin, I. I., and Kortus, J., Beyond Eliashberg Superconductivity in MgB_2: Anharmonicity, Two-Phonon Scattering, and Multiple Gaps, *Phys. Rev. Lett.* 87, 087005, 2001.

[120] Hosseini, A., Harris, R., Kamal, S., Dosanjh, P., Preston, J., Liang, R. X., Hardy, W. N., and Bonn, D. A., Microwave spectroscopy of thermally excited quasiparticles in YBa2Cu3O6.99, *Phys. Rev. B* 60, 1349-1359, 1999.

[121] Corson, J., Orenstein, J., Oh, S., O'Donnell, J., and Eckstein, J. N., Nodal Quasiparticle Lifetime in the Superconducting State of $Bi_2Sr_2CaCu_2O_{8+\delta}$, *Phys. Rev. Lett.* 85, 2569, 2000.

[122] Corson, J., Mallozi, R., Orenstein, J., Eckstein, J. N., and Bozovic, I., Vanishing of phase coherence in underdoped Bi2Sr2CaCu2O8+delta, *Nature* 398, 221 - 223, 1999.

[123] Demsar, J., Averitt, R. D., Taylor, A. J., Demsar, J., Averitt, R. D., Taylor, A. J., Kabanov, V. V., Kang, W. N., Kim, H. J., Choi, E. M., and Lee, S. I., Pair-breaking and superconducting state recovery dynamics in MgB_2, *Phys. Rev. Lett.* 91, 267002-4, 2003.

[124] Kang, W. N., Kim, H. J., Choi, E. M., Jung, C. U., and Lee, S. I., MgB_2 superconducting thin films with a transition temperature of 39 Kelvin, *Science* 292, 1521-1523, 2001.

[125] Carr, G. L., Lobo, R., LaVeigne, J., Reitze, D. H., and Tanner, D. B., Exploring the dynamics of superconductors by time-resolved far-infrared spectroscopy, *Phys. Rev. Lett.* 85, 3001-4, 2000.

[126] Federici, J. F., Greene, B. I., Saeta, P. N., Dykaar, D. R., Sharifi, F., and Dynes, R. C., Direct picosecond measurement of photoinduced Cooper-pair breaking in lead, *Phys. Rev. B* 46, 11153-11156, 1992.

[127] Norman, M. R. and Pepin, C., The electronic nature of high temperature cuprate superconductors, *Rep. Prog. Phys.* 66, 1547, 2003.

[128] Gay, P., Smith, D. C., Stevens, C. J., Chen, C., Yang, G., Abell, S. J., Wang, D. Z., Wang, J. H., Ren, Z. F., and Ryan, J. F., Femtosecond Dynamics of BSCCO-2212, *J. Low Temp. Phys.* 117, 1025, 1999.

[129] Gedik, N., Blake, P., Spitzer, R. C., Orenstein, J., Liang, R., Bonn, D. A., and Hardy, W. N., Single-quasiparticle stability and quasiparticle-pair decay in $YBa_2Cu_3O_{6.5}$, *Phys. Rev. B* 70, 014504, 2004.

[130] Segre, G. P., Gedik, N., Orenstein, J., Bonn, D. A., Liang, R., and Hardy, W. N., Photoinduced Changes of Reflectivity in Single Crystals of $YBa_2Cu_3O_{6.5}$ (Ortho II), *Phys. Rev. Lett.* 88, 137001, 2002.

[131] Averitt, R. D., Rodriguez, G., Lobad, A. I., Siders, J. L. W., Trugman, S. A., and Taylor, A. J., Nonequilibrium superconductivity and quasiparticle dynamics in $YBa_2Cu_3O_{7-\delta}$, *Phys. Rev. B* 63, 140502, 2001.
[132] Averitt, R. D., Thorsmolle, V. K., Jia, Q. X., Trugman, S. A., and Taylor, A. J., Nonequilibrium superconductivity in Y(1-x)PrxBa(2)Cu(3)O(7) thin films, *Physica B* 312, 86-87, 2002.
[133] Kaindl, R. A., Carnahan, M. A., Chemla, D. S., Oh, S., and Eckstein, J. N., Dynamics of Cooper pair formation in $Bi_2Sr_2CaCu_2O_{8+\delta}$, *Phys. Rev. B* 72, 060510(R), 2005.
[134] McElroy, K., Simmonds, R. W., Hoffman, J. E., Lee, D. H., Orenstein, J., Eisaki, H., Uchida, S., and Davis, J. C., Relating atomic-scale electronic phenomena to wave-like quasiparticle states in superconducting $Bi_2Sr_2CaCu_2O_{8+\delta}$, *Nature* 422, 592 - 596, 2003.
[135] Timusk, T. and Statt, B., The pseudogap in high-temperature superconductors: an experimental survey, *Rep. Prog. Phys.* 62, 61-122, 1999.
[136] Kaindl, R., Woerner, M., Elsaesser, T., Smith, D. C., Ryan, J. F., Farnan, G. A., McCurry, M. P., and Walmsley, D. G., Ultrafast mid-infrared response of YBa2Cu3O7, *Science* 287, 470-473, 2000.
[137] Kaindl, R. A., Woerner, M., Elsaesser, T., Smith, D. C., Ryan, J. F., Farnan, G. A., McCurry, M. P., and Walmsley, D. G., Ultrafast mid-infrared response of $YBa_2Cu_3O_{7-\delta}$, *Science* 287, 470-473, 2000.
[138] Kaindl, R. A., Woerner, M., Elsaesser, T., Smith, D. C., Ryan, J. F., Farnan, G. A., McCurry, M. P., and Walmsley, D. G., Femtosecond mid-infrared study of YBa2Cu3O7-delta, *Physica C* 341, 2213-2216, 2000.
[139] Brorson, S. D., Kazeroonian, A., Moodera, J. S., Face, D. W., Cheng, T. K., Ippen, E. P., Dresselhaus, M. S., and Dresselhaus, G., Femtosecond room-temperature measurement of the electron-phonon coupling constant γ in metallic superconductors, *Phys. Rev. Lett.* 64, 2172 - 2175, 1990.
[140] Dagotto, E., Complexity in strongly correlated electronic systems, *Science* 309, 257-262, 2005.
[141] Jin, S., Tiefel, T. H., McCormack, M., Fastnacht, R. A., Ramesh, R., and Chen, L. H., Thousandfold change in resistivity in magnetoresistive La-Ca-Mn-O films, *Science* 264, 413 - 415, 1994.
[142] Anderson, P. W. and Hasegawa, H., Considerations on double exchange, *Phys. Rev.* 100, 675 - 681, 1955.
[143] Jonker, G. H. and van Santen, J. H., Ferromagnetic Compounds of Manganese with Perovskite Structure, *Physica* 16, 337-349, 1950.
[144] van Santen, J. H. and Jonker, G. H., Electrical Conductivity of Ferromagnetic Compounds of Manganese with Perovskite Structure, *Physica* 16, 599-600, 1950.
[145] Wollan, E. O. and Koehler, W. C., Neutron Diffraction Study of the Magnetic Properties of the Series of Perovskite-Type Compounds [(1-x)La,xCa]MnO3, *Phys. Rev.* 100, 545-563, 1955.
[146] Zener, C., Interaction between the d-shells in the transition metals. II. Ferromagnetic compounds of manganese with perovskite structure, *Phys. Rev.* 82, 403-405, 1951.

[147] Millis, A. J., Shraiman, B. I., and Mueller, R., Dynamic Jahn-Teller effect and colossal magnetoresistance in $La_{1-x}Sr_xMnO_3$, *Phys. Rev. Lett.* 77, 175-178, 1996.

[148] Roder, H., Zang, J., and Bishop, A. R., Lattice effects in the colossal-magnetoresistance manganites, *Phys. Rev. Lett.* 76, 1356-1359, 1996.

[149] Ramirez, A. P., Colossal Magnetoresistance, *J. Phys. Cond. Mat.* 9, 8171 - 8199, 1997.

[150] Shimakawa, Y., Kubo, Y., and Manako, T., Giant magnetoresistance in $Tl_2Mn_2O_7$ with the pyrochlore structure, *Nature* 379, 53-55, 1996.

[151] Subramanian, M. A., Toby, B. H., Ramirez, A. P., Marshall, W. J., Sleight, A. W., and Kwei, G. H., Colossal magnetoresistance without Mn3+/Mn4+ double exchange in the stoichiometric pyrochlore Tl2Mn2O7, *Science* 273, 81-84, 1996.

[152] Averitt, R. D., Lobad, A. I., Kwon, C., Trugman, S. A., Thorsmolle, V. K., and Taylor, A. J., Ultrafast conductivity dynamics in colossal magnetoresistance manganites, *Phys. Rev. Lett.* 87, 017401, 2001.

[153] Okamura, H., Koretsune, T., Matsunami, M., Kimura, S., Nanba, T., Imai, H., Shimakawa, Y., and Kubo, Y., Charge dynamics in the colossal magnetoresistance pyrochlore $Tl_2Mn_2O_7$, *Phys. Rev. B* 64, 180409, 2001.

[154] Prasankumar, R. P., Okamura, H., Imai, H., Shimakawa, Y., Kubo, Y., Trugman, S. A., Taylor, A. J., and Averitt, R. D., Coupled charge-spin dynamics of the magnetoresistive pyrochlore $Tl_2Mn_2O_7$ probed using ultrafast midinfrared spectroscopy, *Phys. Rev. Lett.* 95, 267404, 2005.

[155] Quijada, M., Cerne, J., Simpson, J. R., Drew, H. D., Ahn, K. H., Millis, A. J., Shreekala, R., Ramesh, R., Rajeswari, M., and Venkatesan, T., Optical conductivity of manganites: Crossover from Jahn-Teller small polaron to coherent transport in the ferromagnetic state, *Phys. Rev. B* 58, 16093-16102, 1998.

[156] Averitt, R. D. and Taylor, A. J., Ultrafast optical and far-infrared quasiparticle dynamics in correlated electron materials, *J. Phys. Cond. Mat.* 14, R1357-1390, 2002.

[157] Lynn, J. W., Vasiliu-Doloc, L., and Subramanian, M. A., Spin dynamics of the magnetoresistive pyrochlore $Tl_2Mn_2O_7$, *Phys. Rev. Lett.* 80, 4582-4585, 1998.

[158] Butov, L. V., Levitov, L. S., Mintsev, A. V., Simons, B. D., Gossard, A. C., and Chemla, D. S., Formation mechanism and low-temperature instability of exciton rings, *Phys. Rev. Lett.* 92, 117404, 2004.

[159] Prasankumar, R. P., Lee, H. J., Zvyagin, S., Kamenev, K. V., Balakrishnan, G., Mck. Paul, D., Taylor, A. J., and Averitt, R. D., Probing Nanoscale Inhomogeneities through the Polaronic Response, in preparation.

[160] Cavalleri, A., Rini, M., Chong, H. H. W., Fourmaux, S., Glover, T. E., Heimann, P. A., Keiffer, J. C., and Schoenlein, R. W., Band-selective measurements of electron dynamics in VO2 using femtosecond near-edge X-ray absorption, *Phys. Rev. Lett.* 95, 067405, 2005.

[161] Cavalleri, A., Toth, C., Siders, C. W., Squier, J. A., Raksi, F., Forget, P., and Keiffer, J. C., Femtosecond structural dynamics in VO_2 during an ultrafast solid-solid phase transition, *Phys. Rev. Lett.* 87, 237401, 2001.

[162] Hilton, D. J., Prasankumar, R. P., Trugman, S. A., Taylor, A. J., Averitt, R. D., On Photo-Induced Phenomena in Complex Materials: Probing Quasiparticle Dynamics using Infrared and Far-Infrared Pulses, *J. Phys. Soc. Jpn.* 75, 011006, 2006.

[163] Suzuki, T., Sakamaki, T., Tanimura, K., Koshihara, S., and Tokura, Y., Ionic-to-neutral phase transformation induced by photoexcitation of the charge-transfer band in tetrathiafulvalene-p-chloranil crystals, *Phys. Rev. B* 60, 6191-6193, 1999.

[164] Hancock, J. N., McKnew, T., Schlesinger, Z., Sarrao, J. L., and Fisk, Z., Kondo scaling in the optical response of YbIn1-xAgxCu4, *Phys. Rev. Lett.* 92, 186405, 2004.

[165] Demsar, J., Averitt, R. D., Ahn, K. H., Graf, M. J., Trugman, S. A., Kabanov, V. V., Sarrao, J. L., and Taylor, A. J., Quasiparticle relaxation dynamics in heavy fermion compounds, *Phys. Rev. Lett.* 91, 027401-4, 2003.

[166] Feibig, M., Revival of the magnetoelectric effect, *J. Phy. D: Appl.Phys.* 38, R123-R152, 2005.

[167] Hur, N., Park, S., Sharma, P. A., Ahn, J. S., Guha, S., and Cheong, S. W., Electric polarization reversal and memory in a multiferroic material induced by magnetic fields, *Nature* 429, 392 - 395, 2004.

[168] Kimura, T., Lawes, G., and Ramirez, A. P., Electric polarization rotation in a hexaferrite with long-wavelength magnetic structures, *Phys. Rev. Lett.* 94 (13), 137201, 2005.

[169] Lottermoser, T., Lonkai, T., Amann, U., Hohlwein, D., Ihringer, J., and Fiebig, M., Magnetic phase control by an electric field, *Nature* 430, 541 - 544, 2004.

[170] Souchkov, A. B., Simpson, J. R., Quijada, M., Ishibashi, H., Hur, N., Ahn, J. S., Cheong, S.-W., Millis, A. J., and Drew, H. D., Exchange interaction effects on the optical properties of $LuMnO_3$, *Phys. Rev. Lett.* 91, 027203, 2003.

[171] Spaldin, N. A. and Fiebig, M., The renaissance of magnetoelectric multiferroics, *Science* 309, 391-392, 2005.

[172] Pimenov, A., Mukhin, A. A., Ivanov, V. Y., Travkin, V. D., Balbashov, A. M., and Loidl, A., Possible evidence for electromagnons in multiferroic manganites, *Nature Physics* 2, 97-100, 2006.

[173] Axt, V. M. and Kuhn, T., Femtosecond spectroscopy in semiconductors: a key to coherences, correlations, and quantum kinetics, *Rep. Prog. Phys.* 67, 433-512, 2004.

DISCLAIMER